

Gravitational waves from the late inspiral, transition, and plunge of small-mass-ratio eccentric binaries

Devin R. Becker and Scott A. Hughes

Department of Physics and MIT Kavli Institute, MIT, Cambridge, MA 02139 USA

Gaurav Khanna

Department of Physics and Institute for AI & Computational Research,

University of Rhode Island, Kingston, RI 02881 USA

Department of Physics, University of Massachusetts, Dartmouth, MA 02747 USA and

Center for Scientific Computing and Data Science Research,

University of Massachusetts, Dartmouth, MA 02747 USA

Black hole binaries with small mass ratios will be important sources for the forthcoming Laser Interferometer Space Antenna (LISA) mission. Models of such binaries also serve as useful tools for understanding the dynamics of compact binary systems and the gravitational waves they emit. Using an eccentric Ori-Thorne procedure developed in previous work, we build worldlines that describe the full inspiral and plunge of a small body on an initially eccentric orbit of a Kerr black hole. We now calculate the gravitational waves associated with these trajectories using a code that solves the Teukolsky equation in the time domain. The final cycles of these waveforms, the ringdown, contain a superposition of Kerr quasinormal modes followed by a power-law tail. In this paper, we study how a binary’s eccentricity and orbital anomaly angle affect the excitation of both quasinormal modes and late-time tails. We find that the relative excitation of quasinormal modes varies in an important and interesting way with these parameters. For some anomaly angles, the relative excitations of quasinormal modes are essentially indistinguishable from those excited in quasi-circular coalescences. Consistent with other recent studies, we find that eccentricity tends to amplify the late-time power-law tail, though the amount of this amplification varies significantly with orbital anomaly. We thus find that eccentricity has an important impact on the late-time coalescence waveform, but the interplay of eccentricity and orbit anomaly complicates this impact.

I. INTRODUCTION

A. Background, motivation, and past work

Binary black hole mergers detected by the LIGO-Virgo-KAGRA (LVK) Collaboration are, to date, well described using circular coalescence waveform templates [1, 2]. As the LVK gravitational wave (GW) catalog grows, an increasing number of events show evidence of more complicated orbital configurations [3–7]. Looking beyond LVK, small-mass-ratio binaries detectable by future low-frequency GW experiments such as the Laser Interferometer Space Antenna (LISA) [8–10] are expected to enter the detection band in a variety of orbital geometries, with many formation mechanisms predicting substantial eccentricity, even during the merger [11–18].

A merging binary’s coalescence geometry provides critical information about the formation channel which produced the system, a major point of interest for comparable mass systems [19–22] and small-mass-ratio systems [23] alike. Binaries with significant eccentricity are thought to originate from many-body interactions, such as dynamical encounters in dense stellar environments [24–29] and three-body interactions [30–37]. In contrast, aligned-spin systems with small or negligible eccentricity likely form in isolated stellar environments [38–40]. A diagnostic of eccentricity in the late waveform may serve to enhance the power of GW observations to constrain the relative importance of these different channels.

In our previous work, Ref. [41], hereafter BH25, we investigated the impact of orbital eccentricity on the late-time dynamics of black hole binaries in the small-mass-ratio regime. Our model provides a framework for calculating a complete worldline for a small body spiraling into a Kerr black hole as the system emits GWs. A complete worldline requires a prescription for the “transition to plunge” that connects the slowly-evolving, adiabatic portion of the inspiral to the final plunge that rapidly takes the secondary beyond the primary’s event horizon. Our work in BH25 calculates the transition by generalizing the Ori-Thorne procedure [42], originally developed for circular systems, to include eccentricity. Refinement of the eccentric transition is still an active area of research¹. Limitations of the BH25 model include a dependence on *ad hoc* parameter choices, neglect of higher-order contributions from the gravitational self force [57], and relatively slow waveform generation.

Though these limitations must be addressed in order to model transition-to-plunge waveforms faithfully enough to be used to analyze detector data, we are confident that the worldlines generated using BH25 can be used to learn about the late-time dynamics of eccentric binaries and their associated GW signals. Using trajecto-

¹ For additional work on the eccentric transition, see Refs. [43–49] and for transition-to-plunge studies that are not restricted to eccentric systems, see Refs. [42, 50–56].

ries from the framework of BH25, we build the source term for the Teukolsky equation [58], and solve it with the time-domain code of Refs. [59–64] to construct waveforms. Although this work formally applies to extreme mass ratio inspirals (EMRIs), black hole perturbation theory (BHPT) has proven to be a useful tool for understanding the relativistic two-body problem more generally [65–68]. We are hopeful that these results from the small-mass-ratio limit can be used to inform our understanding of eccentric waveform models over a wide range of mass ratios.

We are especially interested in understanding whether eccentricity leaves a unique imprint on a binary’s GW signal. While the impact of eccentricity on inspiral has been studied extensively, work to understand eccentricity’s role in shaping the late-time *ringdown* is ongoing. During ringdown, the binary’s merged remnant emits GWs as it settles to equilibrium [58, 69–71]. First-order perturbation theory predicts that these waves have three main components: a prompt response, followed by a spectrum of quasinormal modes (QNMs), concluding with power-law tails. The prompt response is associated with the initial pulse propagating directly to the observer [72–74]. We do not examine the structure of the prompt response in this work, focusing our analysis on QNMs and power-law tails.

The ringdown is dominated by QNMs, which are modeled as damped sinusoids. In the Regge-Wheeler-Zerilli (RWZ) formalism [75–78] QNMs are associated with poles of the RWZ Green’s function [79]. Observationally, QNMs offer the promise of testing general relativity: a Kerr black hole of mass M and spin a has a known spectrum of QNMs, each with its own frequency and damping time which depends only on M and a . Measuring two QNMs thus completely determines a merged remnant’s mass and spin under the hypothesis that the remnant is a Kerr black hole; measuring more than two QNMs overdetermines the fit and allows one to test the Kerr hypothesis [80–94]. The potential power of QNM measurement also goes beyond their frequencies: the relative amplitude of different QNMs is determined by the late-time geometry of the binary coalescence [95–100]. Previous work in both the small-mass-ratio limit [96, 97, 101], as well as with systems at less extreme mass ratios [98, 99], has shown that the inclination of the binary affects the relative excitation of QNMs. For quasi-circular and nonprecessing mergers in the equatorial plane, the $(\ell, m) = (2, 2)$ fundamental QNM is likely the most dominant excited mode. For significantly misaligned coalescences, the $(2, 1)$ or $(2, 0)$ modes may dominate the spectrum.

This analysis focuses on equatorial orbits, investigating the correspondence between eccentricity and the excited QNM amplitudes. Quasinormal mode excitation from eccentric systems has also been investigated with the effective-one-body (EOB) framework [46, 102], numerical relativity (NR) [103, 104] and first-principles models [79]. Our conclusions in Sec. V outline possible points of synergy between our work and these.

QNMs exponentially decay, and their contribution to the ringdown becomes negligible after some finite number of cycles. Once they have decayed sufficiently, the ringdown is dominated by “Price” tails, in which the GW amplitude decays in a power-law with time [72, 105–107]. These late-time tails are a consequence of gravitational radiation back scattering from the black hole potential. In the RWZ framework, tails arise from a branch cut of the Green’s function along the zero-frequency axis [108–110]. A great deal of work has gone into using tails to learn about the asymptotic structure of dynamical spacetimes and the relaxation of compact objects in general relativity [72, 111–131]. Recently, attention has focused on understanding the impact of a binary’s coalescence geometry on tail excitation. Studies of nonspinning binaries with the RWZ formalism [46, 110], and phenomenological work with BHPT that includes spinning binaries [132, 133] have all found that power-law tails are amplified by a system’s eccentricity: tails take over the ringdown earlier and with larger amplitudes in eccentric systems than in their circular counterparts.

Tails have also been found in NR simulations of comparable-mass binaries: Ref. [134] extracts tails from simulations of head-on collisions, Ref. [135] observes tails in both head-on collisions and highly eccentric mergers, and Ref. [132] points out possible evidence of tails in publicly available Rochester Institute of Technology simulations [136] and data from the Simulating eXtreme Spacetimes (SXS) collaboration [137]². As discussed in Ref. [132], one must be quite careful when looking for tails in NR data. First, publicly available NR simulations typically do not extend into the tail regime of the ringdown; second, simulations have only recently begun to cover the eccentric portion of parameter space where we expect tails to be strongest. (Indeed, defining and controlling eccentricity in NR is fundamentally a challenge; see discussion in Refs. [139–141].) Future improvements to NR studies will likely reduce the necessity for these cautions.

B. This paper: Ringdown from eccentric binary coalescences

An important result of BH25 is that the late-time kinematics of an eccentric binary are sensitive to initial conditions. As the secondary progresses through an eccentric inspiral, it radially oscillates between closest approach to the primary (periapsis) and furthest separation (apoapsis), with these defining orbit points adiabatically evolving due to GW backreaction. We track where the system is in its orbital cycle using an orbital anomaly angle which grows monotonically as inspiral proceeds.

² It’s worth noting that Ref. [132] was published before the most recent update to the SXS catalog, [138], which includes many more eccentric simulations than in previous releases.

BH25 shows that systems which are identical in all initial characteristics except anomaly angle can execute quite different transition-to-plunge dynamics. For example, a system whose secondary passes periapsis and begins returning to apoapsis as the system enters the transition can complete a final radial oscillation before plunging; a system that is identical in all characteristics except the initial anomaly may enter the transition in such a way that the secondary momentarily “whirls” at periapsis before plunging. The final kinematics of the “whirling” system may be barely distinguishable from the behavior of a quasi-circular inspiral. Eccentric systems thus do not display the late-time universality previously shown to describe circular mergers [42, 50, 52]. This sensitivity to the eccentric phase has also been observed in EOB transition-to-plunge trajectories in the test-mass limit [49], as well as NR simulations of symmetric binaries [141].

Not surprisingly, we find that this lack of universality carries over to ringdown excitation as well. In particular, we find that the ringdown does *not* clearly encode a system’s eccentricity. Although the ringdown of an eccentric coalescence can be distinct from the ringdown of a quasi-circular merger, this typically holds only over a range of anomaly as the system enters transition. In most cases we examine, we can find anomaly angles for which ringdown following eccentric inspiral is essentially indistinguishable from quasi-circular ringdown. In particular, we find that systems which follow eccentric inspirals, but whirl in a quasi-circular fashion before plunging, produce ringdown spectra dominated by the $(\ell, m) = (2, 2)$ mode, just as we see in quasi-circular equatorial coalescences. If the anomaly is tuned such that the system does not exhibit this quasi-circular whirling, the $(2, 1)$ mode becomes significant, and can be the dominant mode. This behavior also depends on the system’s spin and eccentricity. We explore these dependencies in Sec. IV B 1.

The diversity of QNM behavior we find from systems that differ only in anomaly angle raises the question of which aspect of the system controls this behavior. We have found there is a particularly strong correlation between the relative mode excitation and the radial velocity during the final plunge. In particular, we find that QNM excitation depends very cleanly on the radial velocity $dr/d\tau$ as the secondary crosses the prograde equatorial light ring [142, 143]. Systems which plunge directly from apoapsis tend to cross the light ring with high radial velocity; those which “whirl” in a quasi-circular manner near periapsis before plunging cross the light ring more slowly (kinematically quite similar to what is seen in a plunge from quasi-circular inspiral). These results, discussed in detail in Sec. IV B 2, indicate that the excitation of ringdown depends mostly on the detailed nature of the secondary’s final plunge trajectory.

Though our main focus is on the excitation of QNMs, we also examine the behavior of the late-time tails which conclude these waveforms. Focusing on the h_{22} spherical mode, we find results broadly consistent with other recent studies of tails from eccentric mergers [46, 110, 132–

134]. In particular, we find that, at fixed anomaly angle, increasing eccentricity e increases the amplitude of the tail, causing it to become the dominant contributor to the waveform earlier. The power-law index describing the decay of the tail remains insensitive to e : tails decay at the same rate, independent of eccentricity. However, our analysis uncovers new phenomenology: the tails vary quite a bit as a function of orbital anomaly.

Reference [133], completed at the same time as the present paper and hereafter called IFK25, presents a far more comprehensive study of the behavior of tails in eccentric mergers, using the same code and methods as we use in this analysis. IFK25 does not examine the influence of the anomaly angle, and uses EOB trajectories to construct their source terms. However, they examine tails for modes with $(\ell, m) = (2, 2), (2, 1), (3, 3), (3, 2), (4, 4)$, and $(4, 3)$. They also use sophisticated Bayesian estimation and MCMC methods to investigate correlations between model parameters, and the impact of the fitting interval on parameter inference. This paper and IFK25 together highlight which system parameters influence the late-time tails of binary waveforms, and clarify how one can reliably extract this contribution to the waves from a binary model.

C. Organization of this paper

The remainder of this paper presents the details of our analysis. We begin in Sec. II by outlining our method for generating eccentric waveforms for small-mass-ratio systems. We start by constructing the worldline that describes the secondary’s inspiral, transition, and plunge into a Kerr black hole. We describe this calculation at length in BH25; Sec. II A summarizes the relevant parts of this analysis, and defines key parameters used to describe the worldlines and their associated waveforms. Section II B then summarizes how we use such a worldline to build the source term for the Teukolsky equation, as well as the computational tools we apply to solve the Teukolsky equation in the time domain.

The main focus of this analysis is the waveform’s ringdown. Section III describes the two ringdown components that we examine, QNMs and power-law tails. We begin with an overview of Kerr QNMs, a discussion of the angular bases used in modeling them, and a description of the algorithm (which follows [96]) that we employ to extract QNMs from our waveforms. We then introduce power-law tails and describe how we model them.

We present results in Sec. IV, starting with QNMs. We first show in Sec. IV A some examples of QNM amplitudes from eccentric prograde and retrograde inspirals into Kerr black holes. This overview gives an introductory sense for how the relative QNM excitation varies with eccentricity, highlighting the spread in mode amplitudes introduced by the initial radial phase. Section IV B 1 explores this dependence on the radial phase in more detail, investigating different spins and a range of

eccentricities. We show that there exists a region of parameter space where the modes are extremely sensitive to the anomaly angle, changing significantly when the angle changes slightly. The dependence on anomaly angle hints at the manner in which plunge geometry controls mode excitation, motivating our study of mode excitation as a function of the secondary’s radial velocity in Sec. IV B 2.

In Sec. IV C, we shift focus to the power-law tails at the end of ringdown. We begin by presenting a typical example of a late-time tail, then examine how tails depend on spin and eccentricity in Sec. IV C 1. This analysis shows that, with all other properties fixed, increasing eccentricity increases the strength of the tails, causing them to dominate ringdown earlier. We then hold eccentricity constant to study the impact of the radial anomaly in Sec. IV C 2. As was the case with the QNMs, we find that varying the radial anomaly has a significant effect on the overall amplitude of late-time tails.

Section V presents our conclusions. Chief among them is that the detailed nature of ringdown in an eccentric coalescence is governed by the final kinematics of the binary as inspiral ends and the system enters its final plunge. These final kinematics in turn are controlled by a combination of parameters, predominantly the binary’s eccentricity and the anomaly angle which determines the radial motion as the secondary transitions from inspiral to plunge. We also discuss ideas for extending this work, and ways to compare with related studies that do not focus on the extreme mass ratio limit.

We include three appendices of technical details which extend our discussion from elsewhere in this paper. Appendix A expands the QNM analysis of Sec. IV B to include modes with $\ell > 2$. The results for these modes are quite similar to what we find for $\ell = 2$; going to higher ℓ has no effect on our conclusions. In Appendix B, we study in greater detail how our results depend on the radial anomaly angle, exploring different mass ratios, as well as connections to related work. Finally, in Appendix C we show that the *ad hoc* parameter choices in the BH25 worldline model do not consequentially impact the excitation of QNMs.

Throughout this work, we use geometrized units with $G = 1$ and $c = 1$. The larger black hole is described by the Kerr metric [144] in Boyer-Lindquist coordinates $\{t, r, \theta, \phi\}$ [145], with mass M and spin parameter a . The smaller body has mass μ , and the mass ratio is $\eta = \mu/M$. We restrict our analysis to orbits in the equatorial plane, where $\theta = \pi/2$.

II. GRAVITATIONAL WAVES FROM SMALL-MASS-RATIO INSPIRAL AND PLUNGE FOR ECCENTRIC ORBITAL CONFIGURATIONS

A. The inspiral, transition, and plunge worldline: How it is computed and key parameters describing it

Our method for calculating an eccentric inspiral, transition, and plunge worldline for a small body spiraling into a Kerr black hole is discussed at length in BH25. Here we give a brief synopsis of this framework, highlighting features that are key to our ringdown study:

1. The small body begins on an eccentric geodesic in the equatorial plane of a Kerr black hole. We initiate the inspiral far enough from the last stable orbit (LSO) to model the dynamics as an *adiabatic inspiral*, where the small body flows through a sequence of geodesic orbits of the large body’s spacetime as the system emits GWs. The rate of flow through this sequence is determined by the flux of GWs at each geodesic, which we extract from precomputed radiation reaction data grids (see Refs. [146–150]).
2. As the secondary approaches the LSO, the GW fluxes grow stronger, and the potential-like function which governs its radial motion grows flatter. The backreaction of GW emission becomes so strong compared to the “restoring force” from the potential’s curvature that the evolution can no longer be described as adiabatic. At this point, the system has begun its *transition to plunge*. We then calculate the trajectory with our eccentric generalization of the procedure introduced by Ori and Thorne [42]. This description of the smaller body’s motion through the transition relies on using the radial geodesic equation (see [151]) with the orbit integrals E and L_z evolving due to backreaction.
3. After crossing the LSO, the small body’s motion is well approximated by a plunging Kerr geodesic with constant E and L_z , which eventually freezes on the primary’s event horizon (as parameterized by Boyer-Lindquist coordinate time).

The top panel of Figure 1 includes a prograde worldline calculated with this procedure. We plot the radial motion as a function of Boyer-Lindquist coordinate time t for a small body’s inspiral, transition, and plunge into a Kerr black hole with $a = 0.7M$, $\eta = 10^{-4}$ and $\epsilon_{\text{IT}} = 0.304$. (The subscript “IT” labels values at the end of adiabatic inspiral and the beginning of the transition.) This system is confined to the equatorial plane of the primary, as is every system discussed in this paper.

Producing worldlines with this method requires two *ad hoc* parameter choices. The first, α_{IT} , determines when adiabatic inspiral ends and the transition begins. It is defined as the ratio of the coordinate acceleration associated with geodesic motion at the inner turning

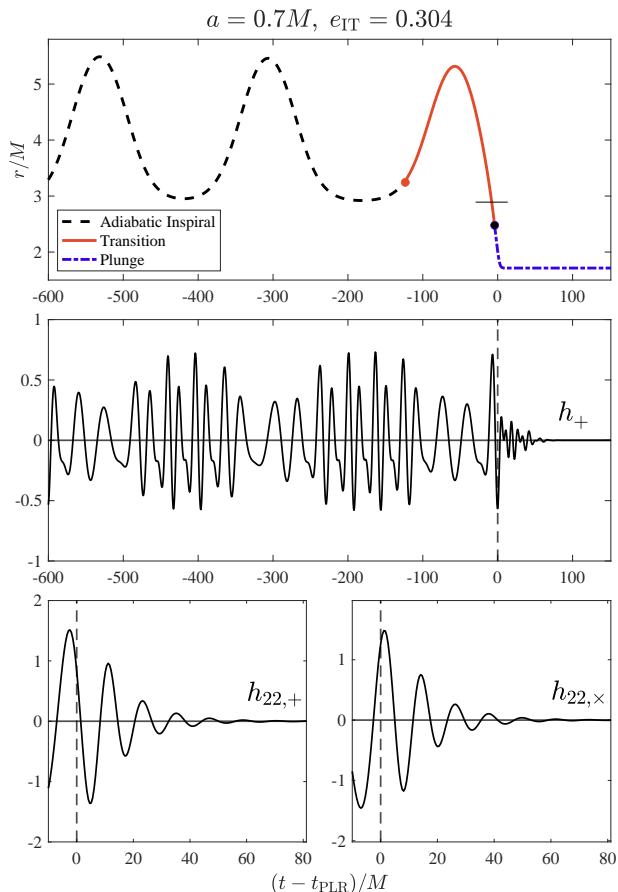


FIG. 1. Example of a prograde inspiral-transition-plunge worldline built using BH25 and its corresponding waveform. The binary has a mass ratio of $\eta = 10^{-4}$ and spin $a = 0.7M$. Top panel shows orbital radius versus Boyer-Lindquist coordinate time. The interval shown includes the final cycles of adiabatic inspiral, ending with an eccentricity of $e_{\text{IT}} = 0.304$. The secondary then completes a radial cycle in the transition, eventually crossing the LSO (the black bar on the plot). Past the LSO, we switch to a plunging geodesic, and the small body ultimately freezes to the horizon coordinate $r_{\text{H}} = 1.7414M$. Before freezing to the horizon, the secondary also crosses the prograde equatorial light ring at t_{PLR} . Middle panel includes the plus-polarization waveform according to an “edge-on” observer in the primary’s equatorial plane. Bottom panels focus on the ringdown of the $\ell = m = 2$ component of the waveform: the bottom left panel is the plus polarization, and the bottom right panel is the cross polarization.

point of the orbit with the acceleration associated with GW-driven backreaction; the exact definition is given in Sec. IIIB of BH25. The second *ad hoc* parameter, β_{TP} , sets where transition ends and plunge begins. This parameter sets a radius between the LSO and the event horizon at which we terminate the transition and treat the secondary’s worldline as a plunging geodesic. As $\beta_{\text{TP}} \rightarrow 0$, the end of the transition approaches the LSO; as $\beta_{\text{TP}} \rightarrow 1$, it approaches the horizon.

Although our transition and plunge worldlines depend

on α_{IT} and β_{TP} , the ringdown does not strongly depend on these parameters. We discuss this in detail in Appendix C, examining how QNM excitation varies with α_{IT} and β_{TP} . It is reassuring that these *ad hoc* parameters do not significantly influence the ringdown sourced by a particular worldline, especially since BH25 noted that the worldline varies moderately with respect to α_{IT} (though the dependence on β_{TP} is quite weak). Nonetheless, it remains dissatisfying that our prescription depends on these arbitrary values; a more fundamental understanding of how eccentric inspiral terminates would be extremely valuable. Reference [47] discusses recent progress in describing the post-adiabatic eccentric inspiral, and is important progress in this vein.

Our transition and plunge trajectories also depend on initial conditions, namely the initial radial anomaly angle, χ_{r0} . Along a geodesic, we can parametrize the radial motion by writing

$$r = \frac{p}{1 + e \cos(\chi_r + \chi_{r0})}, \quad (2.1)$$

where e is the orbit’s eccentricity and p is its semi-latus rectum. When we initiate our adiabatic inspiral, we choose a starting value of the anomaly χ_{r0} . As the secondary moves along the geodesic, the anomaly χ_r progresses from 0 to 2π . For more information on this particular parametrization, see [152].

Trajectories that differ only by χ_{r0} will undergo identical, though out of phase, adiabatic inspirals. However, when the secondary enters the transition, its motion is highly dependent on the radial phase, as this sets the transition’s initial position and velocity. For some values of χ_{r0} , the small body will enter the transition and execute an additional radial oscillation before rapidly plunging into the primary’s horizon; for others, it will “whirl” on a quasi-circular trajectory for some time before plunging. An extensive discussion of the dependence of our transition and plunge trajectories on the relativistic anomaly is included in BH25. In Secs. IV B 1 and IV C 2, we investigate the impact of the initial anomaly angle on the QNMs and tails excited by these systems.

Another useful quantity for assessing the impact of a system’s late-time dynamics on its ringdown is the secondary’s radial velocity as it crosses the prograde light ring (PLR). The location of the light ring depends only on the mass and spin of the primary, occupying the following radius in the equatorial plane:

$$r_{\text{PLR}} = 2M \left[1 + \cos \left(\frac{2}{3} \cos^{-1} \left[-\frac{a}{M} \right] \right) \right]. \quad (2.2)$$

Once the secondary reaches r_{PLR} , we calculate its proper time radial velocity by evaluating the radial geodesic equation at r_{PLR} and with the values of E and L_z at this instant. In the equatorial limit, this velocity is

$$\left(\frac{dr}{d\tau} \right)_{r=r_{\text{PLR}}} = \frac{1}{r_{\text{PLR}}^2} \left[[E(r_{\text{PLR}}^2 + a^2) - aL_z] - \Delta_{\text{PLR}} [r_{\text{PLR}}^2 + (L_z - aE)^2]^{1/2} \right] \quad (2.3)$$

where $\Delta_{\text{PLR}} = r_{\text{PLR}}^2 - 2Mr_{\text{PLR}} + a^2$.

In principle, the velocity at any moment during plunge could serve as a probe of the secondary's late-time dynamics. We choose the PLR crossing in order to have a consistent comparison across systems, though we are also motivated by the role that particle dynamics at the light ring has held in ringdown studies (see, for example, Ref. [142]). We present the relative QNM excitation as a function of the radial velocity at the PLR in Sec. IV B 2.

B. Solving the time-domain Teukolsky equation

Once we construct the inspiral-transition-plunge worldline by way of BH25, we use this worldline to build the source term for the time-domain Teukolsky equation [58]. The Teukolsky equation describes scalar, vector, and tensor field perturbations to Kerr spacetime, with tensor perturbations describing the radiative degrees of freedom of gravity. We schematically write this equation

$$\mathcal{D}^2\Psi = 4\pi\Sigma\mathcal{T}, \quad (2.4)$$

where \mathcal{D}^2 is a second-order differential operator (see [58] for its explicit form), Ψ is related to the Newman-Penrose curvature scalar ψ_4 (see [153]) via $\Psi = r^4\psi_4$ for equatorial orbits, and \mathcal{T} is the source term. We are particularly interested in ψ_4 because at future null infinity

$$\psi_4 = \frac{1}{2} \frac{d^2}{dt^2} (h_+ - ih_\times). \quad (2.5)$$

Hence, far from the source, ψ_4 encodes the emitted GWs.

We compute the source \mathcal{T} in Eq. (2.4) by using our worldline to build the secondary's energy-momentum tensor, which takes the following form in the equatorial limit:

$$T_{\alpha\beta} = \mu \frac{u_\alpha u_\beta}{r^2 u^t} \delta[r - r(t)] \delta[\phi - \phi(t)] \delta[\theta - \pi/2], \quad (2.6)$$

where u^α is the secondary's 4-velocity along its worldline. We then project $T_{\alpha\beta}$ onto certain legs of the Kinnersley tetrad and operate on the resulting expression with a second-order differential operator to get \mathcal{T} ; see [58].

Once we have \mathcal{T} , we solve Eq. (2.4) in the time domain using methods outlined in Refs. [59–64]. The waveforms in the middle and bottom panels of Figure 1 were calculated with this procedure, using the worldline in the top panel as the source. The middle panel gives the full waveform from our numerical code; the bottom panels focus on the ringdown, showing contributions from the plus and cross polarizations of the $(\ell, m) = (2, 2)$ spherical mode. Our code decomposes waveforms as

$$h(t) = \sum_{\ell, m} h_{\ell m}(t) {}_{-2}Y_{\ell m}(\theta, \phi), \quad (2.7)$$

where $h_{\ell m}(t) = h_{\ell m,+}(t) - ih_{\ell m,\times}(t)$, and (ℓ, m) is the spherical mode index. The functions ${}_{-2}Y_{\ell m}$ are -2 spin-weighted spherical harmonics [154]. (We discuss some

issues related to the spherical mode decomposition in Sec. III A 1.)

For the QNM-dominated portion of the ringdown, the GW strain is well above the numerical noise floor of the time-domain Teukolsky solver discussed in Refs. [59–63]. Power-law tails, however, contribute at much lower amplitudes, especially for small eccentricity systems. To perform more extensive studies of the tail behavior in both our work and IFK25, this time-domain solver has been adjusted to resolve waveform features at much lower amplitudes, by, for example, upgrading its infrastructure to support higher-precision floating-point arithmetic [64].

III. DESCRIBING A WAVEFORM'S RINGDOWN CONTENT

The methods outlined in Sec. II produce the time-domain waveform sourced by the inspiral, transition, and plunge of a small body into a Kerr black hole. We now shift our focus to the waveform's final cycles — the ringdown. First-order perturbation theory predicts that the ringdown includes contributions from both QNMs and power-law tails. In this section, we briefly define these ringdown components and summarize the fitting procedures we use to extract them from our waveforms.

A. Quasinormal Modes

In its early stages, the ringdown can be modeled as a linear superposition of QNMs. To understand QNMs more concretely, we first return to the Teukolsky equation (2.4). Teukolsky showed [58] that Eq. (2.4) separates when decomposed in the frequency domain, resulting in ordinary differential equations. The solution for a given mode with frequency $\sigma \in \mathbb{C}$ is then given by

$$\Psi = \sum_{k=2}^{\infty} \sum_{m=-k}^k \sum_{n=0}^{\infty} {}_sR_{kmn}^{a\sigma}(r) {}_sS_{kmn}^{a\sigma}(\theta, \phi) e^{-i\sigma t}. \quad (3.1)$$

By virtue of separability, the radial dependence of the solution is entirely described by ${}_sR_{kmn}^{a\sigma}(r)$, and the angular dependence by ${}_sS_{kmn}^{a\sigma}(\theta, \phi)$. The functions ${}_sS_{kmn}^{a\sigma}$ are spin-weighted *spheroidal* harmonics. When $a = 0$, these simplify to spin-weighted *spherical* harmonics. We discuss the interplay between the spherical and spheroidal harmonic bases in the following subsection. For more information on spherical and spheroidal harmonics, as well as the radial function ${}_sR_{kmn}^{a\sigma}$, see Ref. [155]. The indices k and m give the multipole and azimuthal numbers of the spheroidal harmonics, respectively, and the index n is the overtone number [155, 156]. Note that $\{r, \theta, \phi\}$ in this context is the radius and angular position at which the field is measured, not the binary's orbit position.

For certain frequencies, the modes in Eq. (3.1) satisfy physical boundary conditions: they describe radiation that is purely ingoing at the horizon and purely

outgoing at null infinity. These solutions are the QNMs of the black hole, whose frequencies we denote σ_{kmn} . We can write σ_{kmn} as

$$\sigma_{kmn} = \omega_{kmn} - i/\tau_{kmn}, \quad (3.2)$$

where ω_{kmn} is the oscillation frequency of the QNM, and τ_{kmn} is the mode's damping time.

So long as the product of the merger is a Kerr black hole, the excited QNM frequencies depend only on the mass M and spin a of the merger remnant. In the small-mass-ratio limit, we take both M and a to be the mass and spin of the primary. For a given M and a , we pull ω_{kmn} and τ_{kmn} from the `qnm` Python package [157],

$$h^{\text{QNM}}(t) = \sum_{kmn} [\mathcal{A}_{kmn} e^{-i[\sigma_{kmn}(t-t_0) - \phi_{kmn}]} {}_{-2}S_{kmn}^{a\sigma_{kmn}}(\theta, \phi) + \mathcal{A}'_{kmn} e^{i[\sigma_{kmn}^*(t-t_0) + \phi'_{kmn}]} {}_{-2}S_{kmn}^{a\sigma_{kmn}}(\pi - \theta, \phi)^*]. \quad (3.3)$$

The constants $\{\mathcal{A}_{kmn}, \mathcal{A}'_{kmn}, \phi_{kmn}, \phi'_{kmn}\}$ are the amplitudes and phases associated with the regular mode (unprimed) and its mirror mode (primed) for each (k, m, n) .

We assume the waveform is ringdown dominated when $t \geq t_0$. Note that there is no unambiguous definition for t_0 , especially in the small-mass-ratio regime [159, 160]. Previous work has shown that the extracted QNM amplitudes and phases depend on t_0 ; however, the *relative* modes are largely insensitive to this parameter [159]. Studies focusing on comparable mass systems often use peaks in the waveform's orbital frequency [104] or in the GW amplitude [161–164] to mark the start of ringdown; more recent work has made progress systematically sampling different start times near these regions (cf. [165–172]). However, EMRI systems do not always have a clear peak in either frequency or amplitude. We instead assume ringdown has begun once the secondary crosses the prograde equatorial photon ring [142, 143].

The magnitude of each mode also depends on μ/D , the ratio of the secondary's mass to the distance of the system: $\mathcal{A}_{kmn} \propto \mu/D$. We set $\mu/D = 1$; results can be simply rescaled by introducing the factor μ/D .

1. Spherical and spheroidal expansions

As illustrated by Eq. (2.7), our code that solves the Teukolsky equation decomposes waveforms in a spherical harmonic basis. Since we fit numerical data projected onto a spherical basis to a QNM model in a spheroidal basis, we must take mode mixing into account [173–177]. Mode mixing occurs because basis functions with the same azimuthal index m overlap:

$${}_{-2}S_{kmn}^{a\sigma_{kmn}}(\theta, \phi) = \sum_{\ell} \mu_{m\ell kn}^* (a\sigma_{kmn}) {}_{-2}Y_{\ell m}(\theta, \phi), \quad (3.4)$$

though tools for calculating both ω_{kmn} and τ_{kmn} and tables reporting their values are also included in [82, 155].

As a consequence of the Teukolsky equation's symmetry, QNMs from Kerr black holes come in pairs: for a given set $(k, m; a, M)$, the eigenvalue problem admits two solutions: ${}_sS_{kmn}^{a\sigma_{kmn}}(\theta, \phi)$, with a positive oscillation frequency, and ${}_sS_{k-mn}^{a\sigma_{kmn}}(\pi - \theta, \phi)^*$, with a negative oscillation frequency and a different damping time (where $*$ represents complex conjugation). The latter contributions are called “mirror modes” (see [82, 158]). Taking into account contributions from both regular modes and their mirrors, and specializing to spin weight -2 , we follow [82, 96, 97] and write the QNM contribution to the waveform as

where k is the spheroidal mode index and ℓ is a spherical mode index. The overlap coefficients $\mu_{m\ell kn}$ are included in the Python `qnm` package; they can also be calculated using the algorithm discussed in Appendix A of Ref. [178] (see also Ref. [179]), and are tabulated in [174].

To fold mode mixing into our waveform analysis, we first equate the left-hand side of Eq. (2.7), our numerical data, to the right-hand side of Eq. (3.3), the QNM contribution to the ringdown. We then multiply both sides of the resultant equation by ${}_{-2}Y_{\ell m}^*(\theta, \phi)$, integrate over the sphere, and apply Eq. (3.4). We then find

$$h_{\ell m}(t) = \sum_{k=k_{\min}}^{\infty} \sum_{n=0}^{\infty} [a_{m\ell kn}(t) \mathcal{C}_{kmn} + a'_{-m\ell kn}(t) \mathcal{C}'_{k-mn}], \quad (3.5)$$

where $k_{\min} = \max(2, |m|)$. The constants \mathcal{C}_{kmn} and \mathcal{C}'_{k-mn} encode the QNM amplitudes and phases:

$$\mathcal{C}_{kmn} \equiv \mathcal{A}_{kmn} e^{i\phi_{kmn}}, \quad \mathcal{C}'_{k-mn} \equiv \mathcal{A}'_{k-mn} e^{i\phi'_{k-mn}}, \quad (3.6)$$

and the overlap coefficients are absorbed into the time-dependent coefficients:

$$\begin{aligned} a_{m\ell kn}(t) &= \mu_{m\ell kn}^* (a\sigma_{kmn}) e^{-i\sigma_{kmn}(t-t_0)}, \\ a'_{-m\ell kn}(t) &= (-1)^\ell \mu_{m\ell kn} (a\sigma_{kmn}) e^{i\sigma_{kmn}^*(t-t_0)}. \end{aligned} \quad (3.7)$$

For additional details of the derivation of Eq. (3.5), see Ref. [96].

2. Mode extraction: A quick synopsis

The code we use to extract QNMs from our waveforms was developed for the analysis carried out in [96, 97]. Here we summarize the key features of this algorithm; for a more comprehensive discussion, see Sec. IIIC of [96].

We begin by describing the basic features of the code, as well as the simplifications it makes to the general QNM picture introduced in Sec. III A.

In contrast to similar studies carried out on comparable mass binaries, by working in the small-mass-ratio limit, we know the mass and spin of the remnant black hole *a priori*. Since the mass and spin of the merged remnant determine the expected spectrum of QNMs, the algorithm assumes the ringdown contains those Kerr QNM frequencies and extracts their amplitudes and phases. We also neglect overtone modes, i.e. QNMs for $n \geq 1$. As n increases, the damping time of the mode τ_{kmn} decreases [72]. We assume that by $t - t_0 \gtrsim 25M$, the ringdown is dominated by the fundamental QNMs. The excitation of overtones is an important and interesting topic, but not one that we explore in this work.

In principle, the sum over k in Eq. (3.5) is taken to infinity. In practice, the overlap coefficients peak when $k = \ell$ and then quickly decrease. We thus truncate the sum at a finite value $k_{\max} = \ell + K_\ell$, where K_ℓ is determined by a procedure that we describe momentarily.

These simplifications to our sums over k and n allow us to rewrite Eq. (3.5) as

$$h_{\ell m}(t) = \sum_{k=k_{\min}}^{\ell+K_\ell} [a_{m\ell k 0}(t)\mathcal{C}_{km0} + a'_{-m\ell k 0}(t)\mathcal{C}'_{k-m0}]. \quad (3.8)$$

Using our numerical data, $h_{\ell m}$, we calculate \mathcal{C}_{km0} and \mathcal{C}'_{k-m0} with the iterative fitting routine of [96]. The basic structure of this algorithm is as follows:

1. Begin by picking some number \mathcal{N} of spherical modes (ℓ_i, m) to incorporate into the fit. Set $k_{\min} = \ell_1 = \max(2, |m|)$. The choice of \mathcal{N} determines the number of mixed modes included beyond $\ell = |m|$, thus setting K_ℓ . For example, if we are fitting h_{22} spherical data, choosing $\mathcal{N} = 1$ would only include the $\ell = 2$ modes, while choosing $\mathcal{N} = 3$ includes the $\ell = 2$ modes, as well as the $\ell = 3$ and $\ell = 4$ modes.
2. Evaluate Eq. (3.8) and its time derivative at some $t > t_0$. Solve the resulting $2\mathcal{N}$ linear equations for the mode amplitudes \mathcal{C}_{km0} and \mathcal{C}'_{k-m0} .
3. Repeat the previous step at multiple times in the QNM-dominated regime, again solving for \mathcal{C}_{km0} and \mathcal{C}'_{k-m0} . This tests the consistency of the algorithm: if the values found for \mathcal{C}_{km0} and \mathcal{C}'_{k-m0} are stable, then the ringdown model is consistent with the data $h_{\ell m}$. If the values of \mathcal{C}_{km0} and \mathcal{C}'_{k-m0} are not stable (e.g., their values oscillate over time), then the ringdown model is inadequate. The model may just need more spheroidal modes, so increase \mathcal{N} and repeat the procedure. (It may also be the case that the radiation is not dominated by QNMs; no stable solution will emerge in this case.)
4. Once \mathcal{C}_{km0} and \mathcal{C}_{k-m0} stabilize, calculate a moving average with fixed Δt . Set $\bar{\mathcal{C}}_{km0}$ and $\bar{\mathcal{C}}'_{k-m0}$ to

the average with the least variance. The ringdown model is then given by

$$h_{\ell m}^{\text{RD}}(t) = \sum_{k=k_{\min}}^{\ell+K_\ell} [a_{m\ell k 0}(t)\bar{\mathcal{C}}_{km0} + a'_{-m\ell k 0}(t)\bar{\mathcal{C}}'_{k-m0}]. \quad (3.9)$$

We point the reader to Ref. [96] for more of the computational details of this fitting procedure, as well as consistency checks between this algorithm and previous work.

B. Power-law tails

At sufficiently late times, the ringdown is composed of slowly decaying, power-law tails. In terms of the Teukolsky function ψ_4 , the tail contribution to the ringdown can be modeled as

$$[\psi_4^{\text{tail}}]_{\ell m}(t) = \mathcal{A}_{\psi_{\text{tail}}}^{\ell m}(t + c_{\text{tail}}^{\ell m}) p_{\psi_{\text{tail}}}^{\ell m} e^{i\phi_{\text{tail}}^{\ell m}}, \quad (3.10)$$

where ψ_4 is projected onto the same basis of spherical harmonics we use to describe $h_{\ell m}$. The parameter $\mathcal{A}_{\psi_{\text{tail}}}^{\ell m}$ sets the amplitude of the tail when it begins dominating the waveform, $c_{\text{tail}}^{\ell m}$ is a time-shift parameter, and $p_{\psi_{\text{tail}}}^{\ell m}$ is the power-law index. We expect a power-law index of $p_{\psi_{\text{tail}}}^{\ell m} = -(\ell + 4)$ [116, 180] to describe the decay of $[\psi_4]_{\ell m}$. This differs from the power-law index of tails in $h_{\ell m}$, for which we expect $p_{h_{\text{tail}}}^{\ell m} = -(\ell + 2)$. As we explain in more detail below, we extract tails from $[\psi_4]_{\ell m}$ rather than $h_{\ell m}$ to avoid numerical noise effects which can mask tails in our data. We focus on the $\ell = m = 2$ harmonic mode, for which we expect $p_{\psi_{\text{tail}}}^{22} = -6$. Tails from higher-order spherical modes decay more rapidly, making them difficult to isolate in numerical data. Such contributions, as well as tails from $\ell = 2$ modes with $m \neq 2$, are studied at length in IFK25.

In both our study and that presented in IFK25, the waveforms are extracted at future null infinity. The code directly computes $[\psi_4]_{\ell m}$. By Eq. (2.5), $h_{\ell m}$ can then be found by twice integrating $[\psi_4]_{\ell m}$. This double integration tends to amplify numerical noise. Although this noise is “harmless” for much of our analysis, it is extremely important when attempting to extract tails, especially for low eccentricities for which the amplitude tends to be exceedingly small. (Past work [132] overcame this limitation by studying systems with eccentricity $e > 0.8$.) Because they are simply related by time derivatives (or integrals), either $[\psi_4]_{\ell m}$ or $h_{\ell m}$ can be used to diagnose the properties of tails. One must, however, bear in mind which particular field is used in a given analysis to make sure that one compares like with like between different analyses.

1. Tail extraction: A quick synopsis

We fit the tails using `gw tails`, a Python package developed in Ref. [132] and expanded for IFK25.

Our study applies the portion of `gwtails` that uses `scipy.curve-fit` for a quick estimate of the parameters $\{A_{\psi\text{tail}}, c_{\text{tail}}, p_{\psi\text{tail}}\}$ with nonlinear least-squares optimization. This is sufficient for our initial study. A deeper analysis of late-time tails, such as that given in IFK25, requires a more complete characterization of these parameters, examining their correlations and dependence on the chosen fitting interval. This is done with the update to `gwtails` made with IFK25, which introduces Bayesian inference and MCMC methods to study the fit parameters more thoroughly.

As the QNM contribution decays, the waveform exhibits brief oscillations before the tail dominates. These oscillations arise from QNMs mixing with tails and should be omitted both from the QNM extraction regime and the region considered for tail fits [46, 110, 132, 134, 135]. We consequently begin fitting the power-law tail after the oscillations vanish. This usually occurs when $t - t_{\text{PLR}} \gtrsim 300M - 500M$, though the precise start time varies with eccentricity and the late-time anomaly angle. Ideally, we would start fitting tails even later, but the ringdown data we analyze only extend to $t - t_{\text{PLR}} \approx 1000M$, and good fit convergence typically requires a time range larger than about $300M$. The IFK25 analysis calculates their waveforms to $9000M$ after the merger, so they are able to provide a more complete analysis of how the fitting interval affects tail inference.

IV. RESULTS

A. Mode excitation

Figure 2 catalogs spheroidal QNM excitation for $k = 2$, $m \in \{-2, -1, 0, 1, 2\}$ for a system with mass ratio $\eta = 10^{-4}$ and primary spin $a = 0.3M$. We show both prograde (left) and retrograde (right) plunges. The top panels include results for systems with “small” eccentricity at plunge $e_{\text{IT}} = 0.09$; bottom panels have the moderately large value $e_{\text{IT}} = 0.50$. Because an eccentric inspiral’s late-time dynamics strongly depend on the value of the radial anomaly angle as the secondary enters the strong field, we calculate the mode amplitudes for a range of trajectories. Each panel shows data for the QNM excitation of 36 systems with parameters as described above, and with the anomaly angle at the end of adiabatic inspiral, $\chi_{r\text{IT}} \in [0^\circ, 360^\circ]$. Each data point denotes the sample’s average mode amplitude; the vertical bars show the spread about this average.

Notice that in the small eccentricity case, the spread in mode excitation due to anomaly angle is negligible; the results are in fact very similar to mode excitation for circular and equatorial plunge (compare to the left-hand panel of Fig. 1 of Ref. [97]). At this eccentricity, the strongest $k = 2$ mode for a prograde plunge is $m = 2$; for retrograde configuration, the strongest mode is $m = -2$.

For larger eccentricity, this hierarchy of mode excitation is much less clear. Examining our results for systems

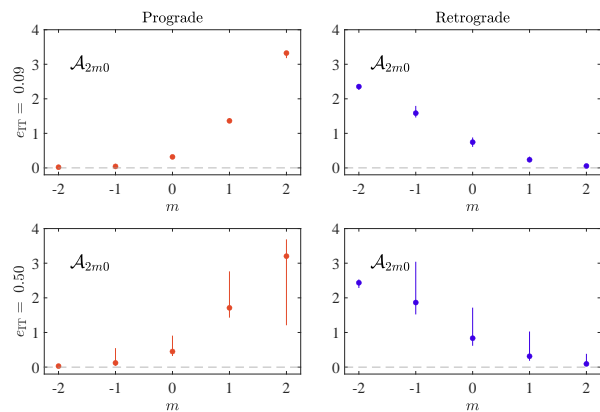


FIG. 2. Prograde (left panels) and retrograde (right panels) spheroidal mode excitations for plunges at $\eta = 10^{-4}$ into a black hole with $a = 0.3M$. All data are for $k = 2$ and $n = 0$ modes, with $m \in \{-2, -1, 0, 1, 2\}$. Top row corresponds to systems with $e_{\text{IT}} = 0.09$; bottom is for $e_{\text{IT}} = 0.50$. The data points denote the average mode excitation across a sample of 36 trajectories that differ only by $\chi_{r\text{IT}}$, and the vertical bars encode the spread in the amplitude from variations in $\chi_{r\text{IT}}$ (the top of the bar gives the maximum amplitude and the bottom of the bar gives the minimum).

with $e_{\text{IT}} = 0.50$, we see that the mean amplitudes indicate that $m = 2$ dominates for prograde systems, and $m = -2$ dominates for retrograde. The range indicated by the vertical bars show that there is a range of $\chi_{r\text{IT}}$ such that $m = 1$ dominates for prograde, and for which $m = -1$ dominates for retrograde. In the next section, we study this dependence on $\chi_{r\text{IT}}$ in more detail, exploring a range of a and e_{IT} .

B. Mode excitation as a function of late-inspiral kinematics

1. Radial anomaly angle

Figure 3 shows spheroidal modes with $k = 2$ for black hole spins $a \in \{0, 0.3M, 0.7M\}$. Each case describes a prograde configuration at mass ratio $\eta = 10^{-4}$ and shows the fundamental mode amplitude \mathcal{A}_{2m0} as a function of $\chi_{r\text{IT}}$. From left to right, the panels include data for $m = -2$ through $m = 2$. Each panel displays QNM amplitudes from systems with four different eccentricities at the end of adiabatic inspiral in the interval $e_{\text{IT}} \in [0.02, 0.56]$ (see the plot legends for precise e_{IT} values). Note that the scale of the vertical axes is different in the panels; this allows us to show the more detailed structure of each mode, though it must be kept in mind that some modes are much higher amplitude than others. Appendix A extends this catalog to $k = 3$ QNMs.

Note the spread in mode amplitude introduced by eccentricity. Red data points show excitation for very small eccentricity and are essentially identical to those found

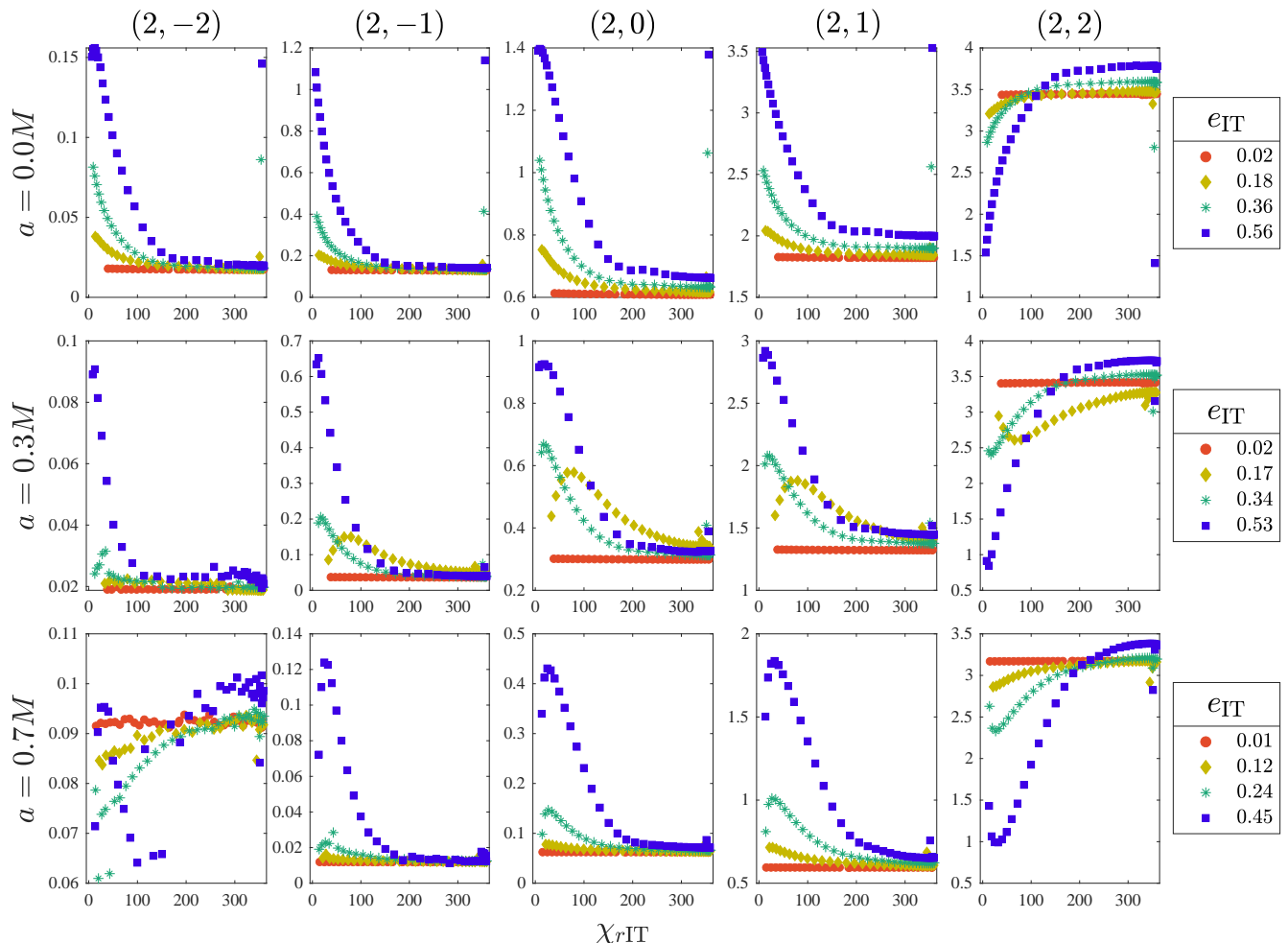


FIG. 3. Mode excitation magnitude $\mathcal{A}_{k m 0}$ for spheroidal QNMs with $k = 2$, $m \in \{-2, -1, 0, 1, 2\}$ and $n = 0$ as a function of the radial anomaly angle at the end of adiabatic inspiral, $\chi_{r\text{IT}}$. Eccentricities in the strong field vary on the range $e_{\text{IT}} \in [0.02, 0.56]$, with red dots denoting the lowest eccentricities, blue squares denoting the highest, and yellow diamonds and green asterisks denoting intermediate values. Top panels show results for black hole spin $a = 0$, middle for $a = 0.3M$ and bottom for $a = 0.7M$. From left to right, m varies from -2 to 2 . Note that the scale of the vertical axes differ between panels. In all cases, the spread in the mode amplitudes increases with eccentricity due to the dependence on $\chi_{r\text{IT}}$.

for quasi-circular inspiral. As eccentricity increases, the mode excitation can deviate significantly from this limit. The data are particularly clear for Schwarzschild (top row): the $(2, 2)$ mode is weakest when $\chi_{r\text{IT}} = 0^\circ$, increasing with this angle until the amplitude plateaus near the quasi-circular value — though changing very suddenly as $\chi_{r\text{IT}} \rightarrow 360^\circ$, enforcing continuity at $\chi_{r\text{IT}} = 0^\circ$. (We discuss this sharp change of behavior in more detail below.) By contrast, modes with $m \neq 2$ are large at $\chi_{r\text{IT}} = 0^\circ$. As this angle grows, these mode amplitudes decrease until they plateau close to the circular limit (modulo wrapping around for continuity as $\chi_{r\text{IT}} \rightarrow 360^\circ$). In all cases, either the $(2, 2)$ or $(2, 1)$ mode is dominant, though which one dominates varies with $\chi_{r\text{IT}}$.

As we increase the primary’s spin, we continue to see that eccentricity modulates QNM amplitudes depending on the value of $\chi_{r\text{IT}}$, though the detailed form is com-

paratively less “clean” than in the Schwarzschild limit. For $a = 0.7M$ (bottom row of Fig. 3), the modes oscillate somewhat as $\chi_{r\text{IT}}$ increases. The $(2, 2)$ mode shows moderately complicated behavior, passing through local extrema as anomaly increases. The general trend, however, is that in eccentric systems, QNM excitation depends in a non-trivial manner on both the eccentricity at the end of inspiral and on the system’s anomaly angle at this moment. For some configurations, mode excitation is similar to the circular limit, with $(2, 2)$ dominating. For some anomaly angles, the $(2, 1)$ mode dominates, and all modes differ substantially from those found in quasi-circular inspiral.

For every spin, and most noticeably for $a = 0$, there is a sharp transition in mode amplitudes near $\chi_{r\text{IT}} = 360^\circ$. This highlights a region of parameter space where the ringdown is particularly sensitive to the anomaly angle.

To capture this behavior in more detail, Fig. 4 zooms in, sampling $\chi_{r\text{IT}}$ more finely. The top panel of Fig. 4 shows four worldlines for systems with $a = 0$, $e_{\text{IT}} = 0.56$ and $\eta = 10^{-4}$. These trajectories differ only in $\chi_{r\text{IT}}$, ranging from $\chi_{r\text{IT}} = 357.50^\circ$ to 357.54° , stepping by $\Delta\chi_{r\text{IT}} \approx 0.01^\circ$. Notice that the time of the final plunge changes by more than $100M$ as the anomaly angle varies over this range. The bottom panels show the amplitudes of the (2, 1) (left) and (2, 2) modes (right) for each system. The systems' terminal kinematics and QNM excitation vary quite significantly as the systems' properties are shifted by a tiny amount.

The worldlines in Fig. 4 reveal a bifurcation in $\chi_{r\text{IT}}$ that shapes the late-time dynamics. This “chifurcation” separates two qualitatively distinct kinematic behaviors: systems whose final kinematics have a quasi-circular character before plunge (cf. the solid red curve in Fig. 4, which sits at $r \simeq 4.5M$ for a time interval of several hundred M before plunging), and systems whose final kinematics take the form of a nearly radial infall from relatively large radius (cf. the dot-dashed blue curve in this figure). These distinct behaviors are reminiscent of critical behavior near the unstable circular orbit (UCO) explored in [49, 181]. In particular, the bifurcation appears to be homoclinic [182, 183], as every trajectory seemingly orbits the UCO, then either plunges immediately or completes an additional radial cycle before plunging. Appendix A of Ref. [49] includes a detailed description of homoclinic orbits of Kerr black holes, highlighting the dependence of these orbits on the relativistic anomaly angle at the LSO. In both our work and Ref. [49], the chifurcation for a nonspinning system appears to occur near the last periaapsis passage, which is consistent with the character of periaapsis, since this is where the secondary switches from moving radially toward the primary to moving away from it. We can also schematically understand this approximate chifurcation location with an effective potential description of the motion (see Ref. [49] for a more detailed discussion of strong-field black hole orbits in effective potentials and their sensitivity to the anomaly angle). In Appendix B, we investigate this behavior in detail with an exploration of how sharply the “chifurcation” depends on mass ratio, and a brief study of the influence of spin and eccentricity at plunge on the location of the chifurcation.

Figure 4 also clarifies an important link between late-time orbital dynamics and relative QNM excitation. Across all spins we have studied, we consistently find that trajectories similar to the solid red trajectory, in which the final kinematics are quasi-circular and followed by a plunge from small radius, tend to be dominated by the (2, 2) QNM. The relative mode excitation in such cases closely resembles the QNM spectrum found in quasi-circular coalescences — consistent with the fact that the final several hundred M of these systems' dynamics are similar to the final orbits of a quasi-circular inspiral.

In contrast, we consistently find that trajectories similar to the blue dot-dashed trajectory, in which the sys-

tem's final moments resemble a direct plunge from relatively large radius with no quasi-circular “whirling,” can result in (2, 1) QNM dominance. In the next section, we make this qualitative observation quantitative by studying the relative mode excitation as a function of the secondary's radial velocity at the PLR crossing.

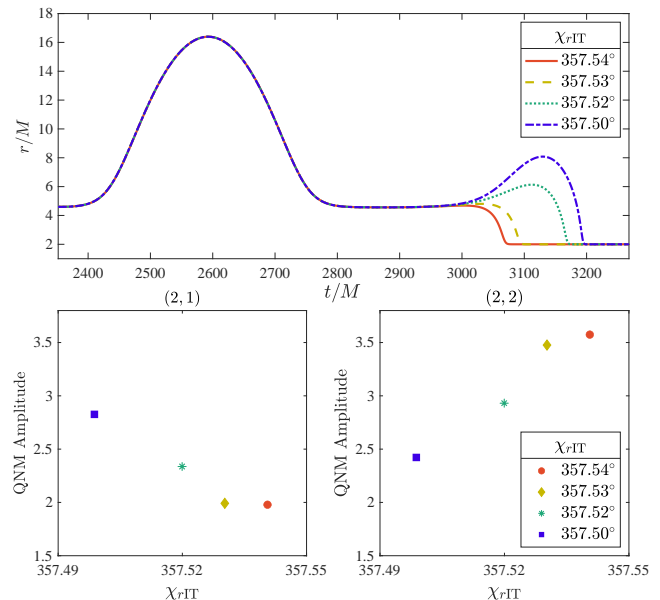


FIG. 4. Worldlines and their resulting mode excitation magnitudes for spheroidal QNMs with $k = 2$, and $m = 1$ or 2 . Top panel includes trajectories for inspirals and plunges into a Schwarzschild black hole with $e_{\text{IT}} = 0.56$ and $\eta = 10^{-4}$. Each trajectory has a slightly different anomaly angle in the strong field delineated by the plot legend ($\Delta\chi_{r\text{IT}} \approx (10^{-2})^\circ$). Bottom panels show the amplitudes of the (2, 1) (left) and (2, 2) mode (right).

2. Mode excitation as a function of the radial velocity at the prograde light ring

Figure 5 shows the same QNM excitation as is shown in Fig. 3, but now presents mode amplitudes as a function of the secondary's radial velocity at the PLR $|dr/d\tau|_{r=r_{\text{PLR}}}$; see Eq. (2.3) for a precise definition of this velocity and Refs. [142, 143] for background on the light ring and its relationship with QNMs. As in Fig. 3, we show the fundamental spheroidal modes with $k = 2$ and $m \in \{-2, -1, 0, 1, 2\}$. Results for $k = 3$ modes are included in Appendix A.

Begin with the $a = 0$ systems (top row of Fig. 5). The amplitude of the (2, 2) mode monotonically declines as $|dr/d\tau|_{r=r_{\text{PLR}}}$ grows; all other modes grow with $|dr/d\tau|_{r=r_{\text{PLR}}}$. We see the same pattern in systems with $a = 0.3M$: as the radial plunge velocity increases, the (2, 2) mode weakens while the other $k = 2$ mode amplitudes grow with $|dr/d\tau|_{r=r_{\text{PLR}}}$. As shown in Appendix

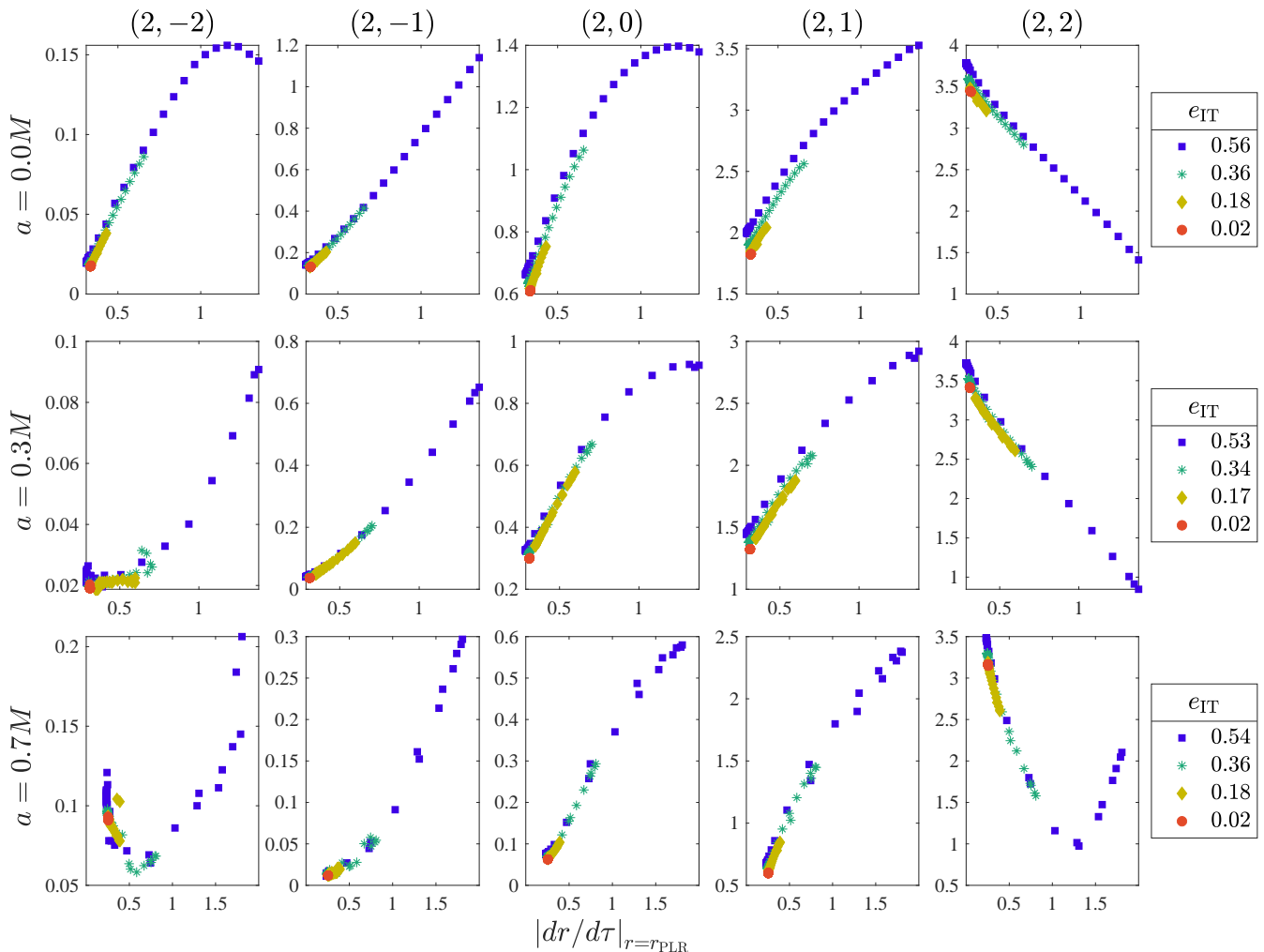


FIG. 5. Mode excitation magnitude \mathcal{A}_{km0} for spheroidal QNMs with $k = 2$, $m \in \{-2, -1, 0, 1, 2\}$, $n = 0$ as a function of the radial velocity at the prograde equatorial light ring, $|dr/d\tau|_{r=r_{\text{PLR}}}$. Eccentricities in the strong field vary on the range $e_{\text{IT}} \in [0.02, 0.56]$, with red dots denoting the lowest eccentricities, blue squares the highest, and yellow diamonds and green asterisks denoting intermediate values. Top panels show results for black hole spin $a = 0$, middle panels $a = 0.3M$ and bottom panels $a = 0.7M$. From left to right, m varies from -2 to 2 . Note that the scale of the vertical axes differs between panels.

A, we tend to find analogous behavior among the $k = 3$ QNMs: the amplitude of the $(3, 3)$ mode falls for high plunge velocities, while other $k = 3$ modes grow.

Increasing spin to $a = 0.7M$ introduces new behavior, at least for large eccentricity. Systems with $e_{\text{IT}} \in \{0.02, 0.18, 0.36\}$ follow the trends described above: the $(2, 2)$ amplitudes decrease as $|dr/d\tau|_{r=r_{\text{PLR}}}$ increases, while the other m modes grow. However, for the $e_{\text{IT}} = 0.54$ case, we see that the $(2, 2)$ mode decreases until $|dr/d\tau|_{r=r_{\text{PLR}}} \simeq 1.3$, at which point its evolution turns around and it increases as $|dr/d\tau|_{r=r_{\text{PLR}}}$ grows. (The other $k = 2$ modes evolve in a fairly monotonic fashion, mostly increasing with radial plunge velocity.) It is worth noting that these cases correspond to the highest plunge velocities found in this sample. It appears that as the plunge velocity gets very large, these systems excite

more complicated QNM spectra.

C. Tail Excitation

We begin our study of the late ringdown by presenting a typical Price tail from our dataset and its power-law fit. Figure 6 shows the post-merger amplitude $[\psi_4]_{22}$ sourced by a small body merging with a Schwarzschild black hole at eccentricity $e_{\text{IT}} = 0.727$ and mass ratio $\eta = 10^{-4}$. The secondary ends its adiabatic inspiral at $\chi_{\text{rIT}} = 89^\circ$; In Sec. IV C 2, we explore how this system's tail varies with χ_{rIT} . Focus first on the mode's amplitude, the solid yellow line. For $t \in [t_{\text{PLR}}, t_{\text{PLR}} + 150M]$, the amplitude rapidly drops as QNMs decay. After this point, but before $t \approx t_{\text{PLR}} + 300M$, the ringdown is

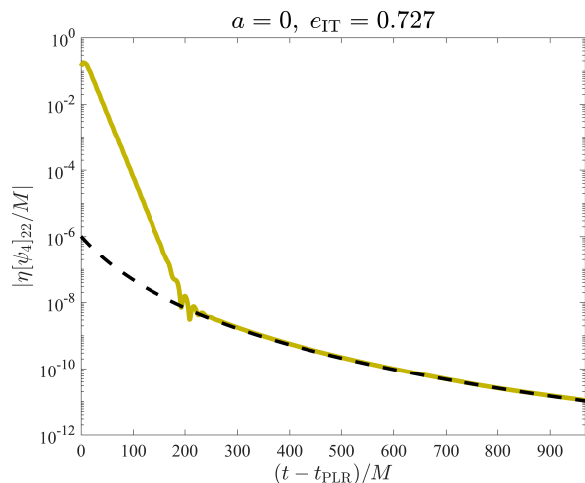


FIG. 6. Ringdown amplitude from a merger with $a = 0$, $\eta = 10^{-4}$, $e_{\text{IT}} = 0.727$ and $\chi_{r\text{IT}} = 89^\circ$. The solid yellow line traces the amplitude of $[\psi_4]_{22}$ as a function of time past the PLR crossing. The black dashed curve represents a fit of the late-time tail to a model with $\mathcal{A}_{\psi_{\text{tail}}}^{22} = 3.28 \times 10^5 \pm 2.7 \times 10^3$, $c_{\text{tail}}^{22} = 132 \pm 0.11$ and $p_{\psi_{\text{tail}}}^{22} = -5.42 \pm 1.1 \times 10^{-3}$.

in an oscillatory regime where QNM and tail contributions mix. We exclude this region, as well as the preceding QNM-dominated region, from our tail fit. Once $t \gtrsim t_{\text{PLR}} + 300M$, the waveform shows a clear power-law decay as the system settles into equilibrium. We model this portion of the ringdown with Eq. (3.10); the dashed black line in Fig. 6 shows the fit we find. On the interval $t - t_{\text{PLR}} \in [300M, 750M]$, we find $\mathcal{A}_{\psi_{\text{tail}}}^{22} = 3.28 \times 10^5 \pm 2.7 \times 10^3$, $c_{\text{tail}}^{22} = 132 \pm 0.11$ and $p_{\psi_{\text{tail}}}^{22} = -5.42 \pm 1.1 \times 10^{-3}$. When we start the fit at later times, the power-law index increases toward its expected value of -6 . We do not undertake a detailed analysis with different fitting intervals here; see IFK25 for such an analysis, specifically with respect to the asymptotic behavior of the power law.

1. Tails as a function of eccentricity and spin

Figure 7 shows the ringdown amplitude after the PLR crossing for binaries in a variety of orbits, all with $\eta = 10^{-4}$ and $\chi_{r\text{IT}} = 115^\circ$. Each system in the left-hand panel has $a = 0$; each curve presents a different eccentricity from the set $e_{\text{IT}} \in \{0.18, 0.37, 0.54, 0.69\}$. The right-hand panel shows results from systems with $a = 0.7M$, but are otherwise identical to those on the left.

We fit each of these tails to a power law; Table I gives the values of $\mathcal{A}_{\psi_{\text{tail}}}$, c_{tail} , and $p_{\psi_{\text{tail}}}$ we find fitting on the interval $t - t_{\text{PLR}} \in [t_{\text{start}}, 1000M]$, where t_{start} is tabulated for each system. For both spins, there is a clear correlation between eccentricity and tail amplitude, at least at fixed radial anomaly: larger eccentricity means larger tail amplitude. This eccentricity-induced

tail amplification is in complete agreement with Refs. [46, 110, 132, 134] and IFK25. Also in line with these studies, we find that the tail dominates the ringdown earlier for systems with higher eccentricities.

The final fit parameter we consider, $p_{\psi_{\text{tail}}}$, does not vary significantly as eccentricity changes, except for the Schwarzschild $e_{\text{IT}} = 0.18$ ringdown, where the slope associated with the power law is slightly more shallow than in our other systems. The deviations we find could simply result from our choice of fitting interval for each system, since the differences we observe are of a similar order of magnitude to those expected from fitting interval shifts; see discussion in Ref. [132] and in IFK25. Regarding the tail's dependence on spin, our results indicate that while spin does affect power-law tails, the specific relationship is not straightforward. For $e_{\text{IT}} = 0.54$ and $e_{\text{IT}} = 0.69$, the tails for the $a = 0$ and $a = 0.7M$ systems are nearly indistinguishable despite notable differences in the QNM and oscillatory regions. Note that IFK25 investigates systems with higher spins than we display here, finding particularly strong tails for retrograde captures into black holes with $a = 0.9M$.

2. Tails as a function of the radial anomaly angle

We next examine power-law tails from a set of eccentric binaries, holding all parameters fixed except the late-time radial anomaly angle $\chi_{r\text{IT}}$. Both panels of Fig. 8, describe systems with $a = 0$, $e_{\text{IT}} = 0.727$, and $\eta = 10^{-4}$. The left-hand panel shows the post-merger amplitude $[\psi_4]_{22}$ as a function of time after the PLR crossing sourced by the worldlines shown in the right-hand panel. These binaries are distinct both in their late-time behavior and their excited ringdown amplitudes, despite the fact that they only differ by $\chi_{r\text{IT}}$. Table II gives the tail parameters we find for these systems. Visual inspection of the tails paired with the fit parameters we find shows that a binary's terminal dynamics strongly shapes the morphology of its power-law tail.

Systems that end with a radial plunge from a large radius (the solid red and dashed yellow trajectories) excite stronger tails than systems that complete quasi-circular whirls before plunging (the dotted green curve and dot-dashed blue curve). Moreover, there appears to be a relationship between the time spent executing quasi-circular whirls and the amplitude of the excited tail, as the system with the longest quasi-circular whirl excites the tail with the lowest amplitude (note that $\mathcal{A}_{\psi_{\text{tail}}}$ is inversely related to the amplitude of the tail when it decouples from the oscillatory regime).

The variations in $\mathcal{A}_{\psi_{\text{tail}}}$ and c_{tail} that arise from changes in $\chi_{r\text{IT}}$ emphasize that neither eccentricity e_{IT} nor radial anomaly $\chi_{r\text{IT}}$ is enough to determine a system's tail: the impact of these parameters on the tail is strongly correlated. Notice that the four tails shown here asymptotically decay with very similar slopes, though a more thorough analysis extending deeper into the ring-

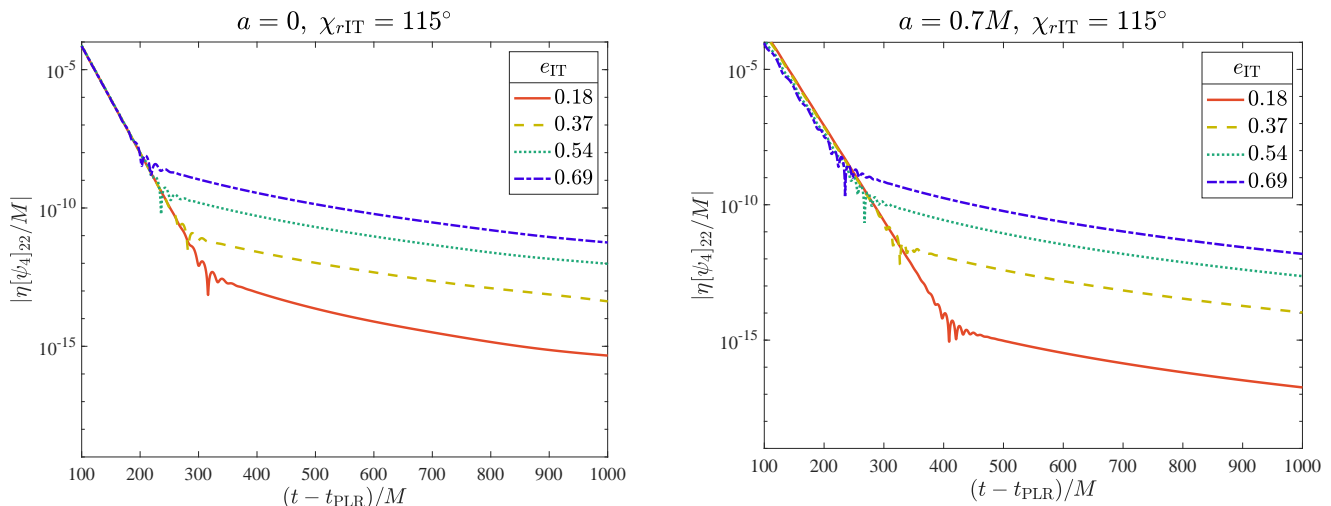


FIG. 7. Power-law tails as a function of eccentricity at the end of adiabatic inspiral. In each case, $\chi_{r\text{IT}} = 115^\circ$ and $\eta = 10^{-4}$. Left panel shows results for secondary’s plunging into a Schwarzschild black hole; Right panel shows results for secondary’s plunging into a Kerr black hole with $a = 0.7M$.

a/M	e_{IT}	$\mathcal{A}_{\psi\text{tail}}$	c_{tail}	$ p_{\psi\text{tail}} $	t_{start}/M
0	0.18	3.68 ± 0.08	-45.9 ± 0.28	$5.36 \pm 3.1 \times 10^{-3}$	434
0	0.37	$1.55 \times 10^4 \pm 574$	79.4 ± 0.60	$5.72 \pm 4.9 \times 10^{-3}$	404
0	0.54	$8.50 \times 10^4 \pm 1.9 \times 10^3$	161 ± 0.33	$5.55 \pm 3.0 \times 10^{-3}$	340
0	0.69	$2.48 \times 10^6 \pm 1.7 \times 10^4$	169 ± 0.09	$5.76 \pm 9.2 \times 10^{-4}$	319
0.7	0.18	7.45 ± 0.04	22.8 ± 0.08	$5.86 \pm 6.8 \times 10^{-4}$	602
0.7	0.37	935 ± 0.88	61.1 ± 0.02	$5.61 \pm 1.3 \times 10^{-4}$	502
0.7	0.54	$1.69 \times 10^4 \pm 12$	50.4 ± 0.01	$5.59 \pm 9.7 \times 10^{-5}$	413
0.7	0.69	$1.18 \times 10^6 \pm 1.5 \times 10^3$	-173 ± 0.02	$5.89 \pm 1.7 \times 10^{-4}$	401

TABLE I. Power-law tail fit parameters for the systems displayed in Fig. 7.

down is needed to ascertain whether they asymptote to the expected value $p_{\psi\text{tail}} = -6$. We outline plans for a more detailed study of the relationship between the tail morphology and the plunge dynamics in our conclusions.

V. CONCLUSIONS AND NEXT STEPS

In this analysis, we have investigated how orbital eccentricity and the radial anomaly angle affect late-time waveforms from binary black hole coalescences in the small-mass-ratio limit. We construct inspiral-transition-plunge worldlines with the BH25 procedure for eccentric small-mass-ratio binaries, then generate the gravitational waveforms produced by these worldlines using a time-domain Teukolsky equation solver. We focus on the final ringdown cycles of these waves, seeking to understand whether eccentricity leaves a distinguishable imprint on the excitation of Kerr QNMs and the late-time Price tails. We find that eccentricity can influence QNM amplitudes

and the structure of the tail, but the details of this influence are complicated by dependence on the strong-field radial anomaly angle. This result is not surprising: our previous work studying eccentric dynamics, BH25, found that the kinematics of the late inspiral and plunge of eccentric systems depend strongly on the anomaly. Some eccentric binaries merge after a final cycle which terminates in a plunge from large radius; others plunge from small radius following some number of quasi-circular whirls. The radial anomaly angle at which the secondary enters the strong field controls which of these possibilities the secondary undertakes, which in turn determines the nature of the system’s ringdown.

Secondaries that plunge immediately after completing quasi-circular whirls excite QNM spectra that closely mimic the mode structure of purely quasi-circular mergers. In particular, the (2, 2) mode dominates. These systems can have significant eccentricity during the inspiral, but if inspiral ends at an anomaly angle such that the system whirls at periaapse before plunging, the ringdown

$$a = 0, e_{\text{IT}} = 0.727$$

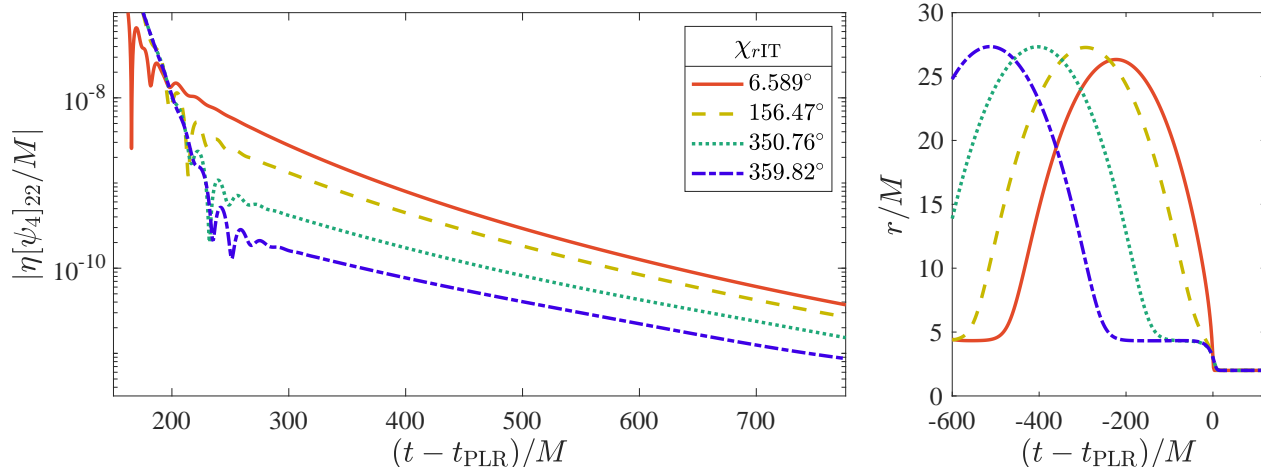


FIG. 8. Left panel: $[\psi_4]_{22}$ ringdown amplitude for four nonspinning binaries, all with $e_{\text{IT}} = 0.727$ and $\eta = 10^{-4}$, but different values of the radial anomaly angle in the strong field. Right panel: the worldlines associated with the ringdown amplitudes in the left panel.

$\chi_{r\text{IT}}$ [deg]	$\mathcal{A}_{\psi\text{tail}}$	c_{tail}	$ p_{\psi\text{tail}} $	t_{start}/M
6.589	$1.44 \times 10^5 \pm 1.2 \times 10^3$	90.0 ± 0.12	$5.31 \pm 1.1 \times 10^{-3}$	400
156.47	$1.81 \times 10^6 \pm 6.2 \times 10^4$	187 ± 0.58	$5.65 \pm 4.5 \times 10^{-3}$	425
350.76	$4.27 \times 10^8 \pm 7.0 \times 10^7$	422 ± 3.2	$6.32 \pm 2.1 \times 10^{-2}$	435
359.82	$1.42 \times 10^{10} \pm 5.7 \times 10^9$	591 ± 8.6	$6.77 \pm 5.0 \times 10^{-2}$	445

TABLE II. Power-law tail fit parameters for the systems displayed in Fig. 8.

appears quasi-circular. If the same secondary approaches the strong field with a different anomaly, it may instead plunge from large radius after a final radial cycle. In this case, the spectrum is dominated by the (2, 1) QNM. In addition to depending on anomaly angle, these behaviors depend on the system’s spin. High spins make (2, 1) dominance possible at lower eccentricities.

In a similar vein, we find that the power-law tails from systems that plunge from large radius have larger amplitudes and earlier start times than systems that execute quasi-circular whirls right before plunge. Though eccentricity can amplify the power-law tail, as found by many related works [46, 110, 132, 134], the anomaly angle also impacts the tail morphology. This indicates that the eccentricity-based amplification is fundamentally determined by a binary’s detailed terminal dynamics, rather than simply the value of its eccentricity.

A key parameter controlling an eccentric coalescence’s ringdown appears to be the velocity of the final plunge. This velocity is in turn influenced by the primary’s spin, orbital eccentricity, and the late-time anomaly. We find a clear relationship between the plunge’s radial velocity through the prograde light ring and the excitation of $k = 2$ QNMs: the amplitude of the (2, 2) mode decreases as this velocity increases, and all other $k = 2$

modes grow with plunge velocity. Systems that merge after quasi-circular whirls typically result in plunges with lower radial velocities, and are dominated by the (2, 2) QNM. Systems that plunge from large radius after a final radial oscillation cross the light ring with quite large radial velocity, and the (2, 1) QNM tends to dominate. As other studies of eccentric waveforms using alternate frameworks and other mass ratios (cf. Refs. [49, 103, 141]) examine the relative excitation of QNMs, we look forward to cross-checking results and investigating how well these results hold up as a function of mass ratio.

A natural direction for future work is to combine this analysis with that of Refs. [52, 96] and BH25 to investigate the relative excitation of QNMs from systems with generic orbital configurations — systems that are both eccentric and inclined. In Sec. VII of BH25, we outline our plan to use [52] to update our eccentric transition-to-plunge procedure to describe inclined systems, thereby allowing the production of generic inspiral-transition-plunge worldlines. Calculating these generic worldlines requires generic radiation reaction data grids, which are now under development for LISA mission data studies (e.g. [150]). Once generic worldlines exist, it will not be difficult to construct their associated waveforms with the Teukolsky equation, and use the algorithm of [96]

to study the relative QNM excitation. We are particularly interested in assessing potential degeneracies between inclination and eccentricity in the QNM hierarchy. When studied independently, it appears that inclination can leave a stronger imprint on the QNM spectrum than eccentricity. A comprehensive study that includes both of these orbital parameters could verify if this is indeed the case, as well as help to uncover what precisely can be learned about a binary’s coalescence geometry from the ringdown alone.

Another key area of interest across mass ratios is the QNM excitation from binaries where both black holes are spinning, especially in cases with spin precession. The self-force community has made excellent progress in recent years in calculating inspiral waveforms from spinning bodies orbiting Kerr black holes (see, for example, Refs. [184–187]). As these studies finalize the details of the inspiral, we can begin working towards a description of the transition to plunge of a spinning body, and eventually apply such a description to a ringdown study.

A more detailed understanding from the perturbative limit of late-time spin precession may be a useful tool for informing NR studies, which have shown that highly precessing systems can excite the $(2, \pm 1)$ and $(2, 0)$ fundamental QNMs [99, 100, 188]. Since eccentricity and inclination can also add power to these specific QNMs, a fully generic study that includes spin precession would of course be ideal. This work could be useful for informing analyses of high-mass GW events such as GW190521 [189] and GW231123 [190], as the GW signals from both of these events may show evidence of spin precession. Studies of these systems thus far have been limited by the small number of inspiral cycles in the LVK band, increasing the importance of the ringdown in uncovering the progenitors of high-mass LVK binaries.

It may also be valuable to undertake a systematic study of how the power-law tails depend on, and presumably encode, the binary’s late-time kinematics. The tail-fitting algorithm developed in IFK25 could be used to examine how the combined dependence on radial anomaly angle and eccentricity influences the behavior of the parameters which describe the tail. Because we find that the tail depends most strongly on the final inspiral and plunge kinematics, it is plausible that a clean dependence on the radial velocity during the plunge exists as well.

ACKNOWLEDGMENTS

We thank Halston Lim for assisting with our implementation of the quasinormal mode extraction pipeline described in Ref. [96]. D.R.B. and S.A.H. acknowledge support from NSF Grants No. PHY–2110384 and PHY–2409644. G.K. acknowledges support from NSF Grants No. PHY–2307236 and DMS–2309609. We also thank Tousif Islam and Guglielmo Faggioli for sharing a draft of Ref. [133] with us, and engaging in much helpful discussion. Computations used GNU Parallel [191], MIT Kavli

Institute resources at MIT’s **engaging** computing cluster, **subMIT** resources at MIT Physics, and the UMass-URI **UNITY** HPC/AI cluster at the Massachusetts Green High Performance Computing Center (MGHPCC).

Appendix A: Higher Order Mode Excitation

In this appendix, we catalog higher-order mode excitation for the systems explored in Sec. IV B. Figure 9 shows the relative QNM amplitudes for fundamental spheroidal modes with $k = 3$ and $m \in \{-3, \dots, 3\}$ as a function of the radial anomaly angle at the end of adiabatic inspiral. Every system has $\eta = 10^{-4}$ and $e_{\text{IT}} \in [0.02, 0.56]$. Top panels focus on binaries with $a = 0$, middle panels have $a = 0.3M$, and bottom panels have $a = 0.7M$. As was the case with the $k = 2$ spheroidal modes, Fig. 9 showcases the spread in the absolute QNM amplitudes sourced by variations in χ_{rIT} .

To connect the relative QNM excitation to the binary’s coalescence dynamics, Fig. 10 shows the same spheroidal mode amplitudes from Fig. 9 as a function of the secondary’s radial velocity at the prograde light ring, $|dr/d\tau|_{r=r_{\text{PLR}}}$. Focusing first on the nonspinning results in the top panels, the relationship between the QNM amplitudes and the plunge velocity is clear: larger radial velocities through the light ring add power to every mode but $(k, m) = (3, 3)$, which dominates the $k = 3$ excitation for quasi-circular mergers. This pattern echoes what we observed in the $k = 2$ mode excitation: the dominant $k = 2$ mode in the quasi-circular case, the $(2, 2)$ mode, is less excited when the secondary rapidly passes through the light ring, while all other $k = 2$ modes gain power.

Combining our $k = 2$ and $k = 3$ results allows us to take a more detailed inventory of eccentric QNM excitation. In nonspinning systems whose final orbital cycles have the character of quasi-circular whirls and in which the systems cross the light ring with relatively low plunge velocity, the $(2, 2)$ QNM dominates, followed by the $(2, 1)$ mode and then $(3, 3)$. Systems that execute a final radial cycle then plunge from large radius tend to dominantly excite $(2, 1)$, then $(2, 2)$, followed by $(3, 2)$ and $(3, 3)$; it is worth noting that we only observe this QNM hierarchy when $e_{\text{IT}} \gtrsim 0.5$ for $a = 0$. Increasing the spin of the primary to $a = 0.7M$ does not alter the leading mode, but the ordering of the subdominant modes can shift, with the $(3, 3)$ mode surpassing the $(2, 1)$ when the final kinematics before plunge are quasi-circular. The detailed dependence of both the $(2, 2)$ and $(3, 3)$ modes on $|dr/d\tau|_{r=r_{\text{PLR}}}$ increases in complexity for higher spins and plunge velocities, making the subdominant QNM hierarchy for systems that plunge from large radius less straightforward. Also note that for $a = 0.7M$, eccentricities as low as $e_{\text{IT}} \approx 0.35$ can produce a QNM spectrum that is discernible from the quasi-circular case if the radial anomaly allows us to distinguish the late-time coalescence kinematics.

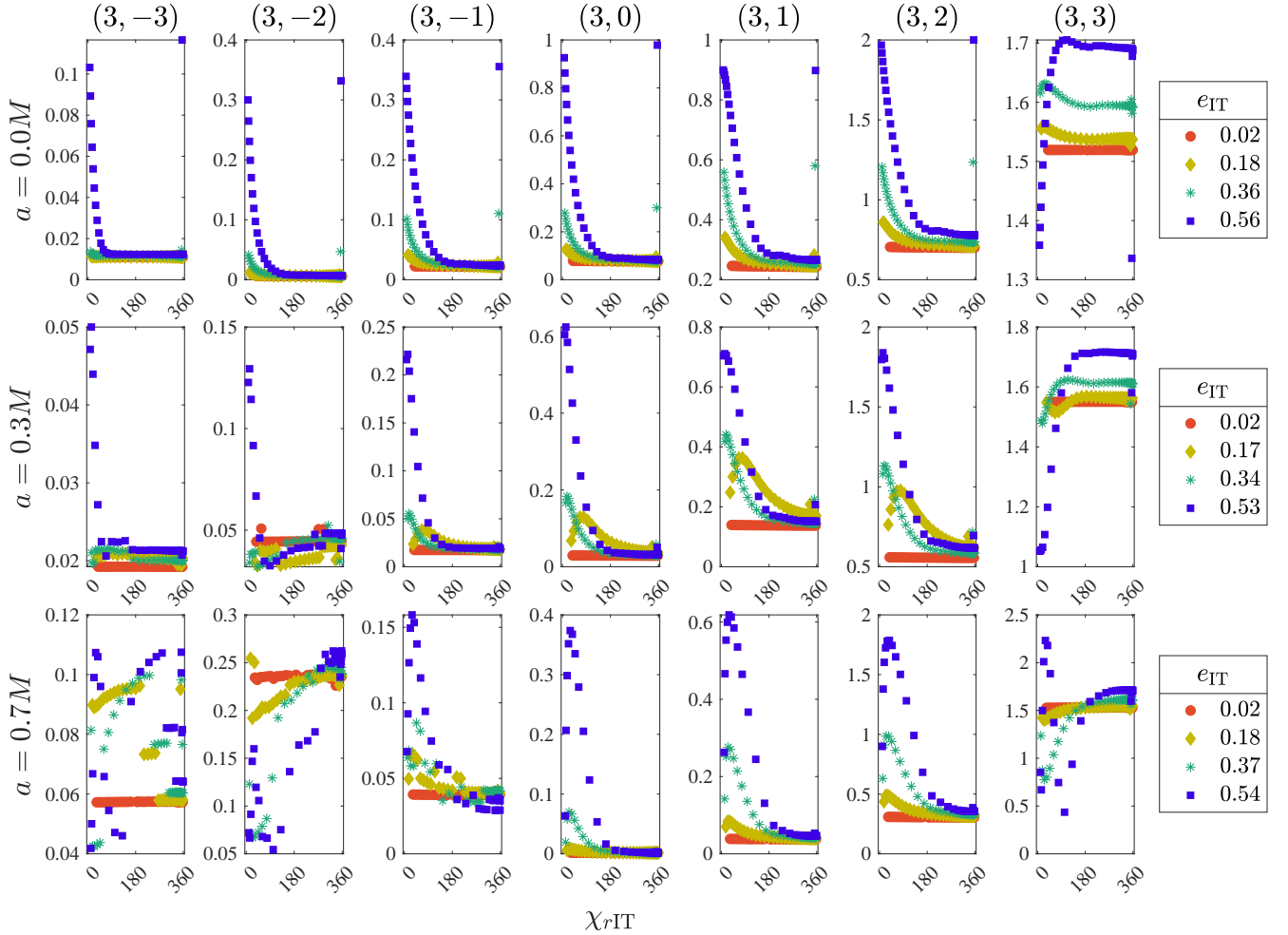


FIG. 9. Mode excitation magnitude \mathcal{A}_{km0} for spheroidal QNMs with $k = 3$, $m \in \{-3, -2, -1, 0, 1, 2, 3\}$, $n = 0$ as a function of radial anomaly at the end of adiabatic inspiral, $\chi_{r\text{IT}}$. Eccentricities in the strong field vary on the range $e_{\text{IT}} \in [0.01, 0.56]$. Red dots denote the lowest eccentricities, blue squares the highest, and yellow diamonds and green asterisks denote intermediate values. Top panels show results for black hole spin $a = 0$, middle panels $a = 0.3M$, and bottom panels $a = 0.7M$. From left to right, m varies from -3 to 3 . Note that the scale of the vertical axes differs between panels.

Appendix B: “Chifurcation”

In Sec. IV, we explored the excitation of QNMs and late-time tails as a function of the radial anomaly at the end of adiabatic inspiral, $\chi_{r\text{IT}}$. Ringdowns from eccentric systems that differ only by $\chi_{r\text{IT}}$ can present distinct QNM amplitudes and tail morphologies. Further, in Sec. IV B 1 we found a region of parameter space in which the worldline is especially sensitive to $\chi_{r\text{IT}}$, resulting in a bifurcation in the late-time kinematics that is particularly consequential to the ringdown. This bifurcation with respect to $\chi_{r\text{IT}}$, which we have dubbed the “chifurcation,” represents an extreme case of an eccentric inspiral’s sensitivity to initial conditions. In this appendix, we study the chifurcation in more detail, first focusing on its dependence on the binary’s mass ratio.

Figure 11 examines the relationship between the chi-

furcation and the mass ratio of the binary. Each worldline shown in Fig. 11 describes a system with $a = 0$ and $e_{\text{IT}} = 0.56$. Those presented in the top panel have $\eta = 10^{-3}$; those in the bottom have $\eta = 10^{-5}$. Both mass ratios exhibit the behaviors separated by the chifurcation: orbits that complete quasi-circular whirls at plunge, the solid red line in both panels, and orbits that plunge after retreating to large radii, the dashed blue curves. Trajectories with anomaly angles in between the given values either whirl slightly longer than the solid red trajectory, or execute an additional radial cycle with a smaller amplitude than the dashed blue curve (see Fig. 4 for examples of this intermediate behavior). For example, if one of the systems in the top panel instead had $\chi_{r\text{IT}} = 10^\circ$, it would execute a radial cycle to about $r = 11M$ before plunging. For the dashed blue trajectories, we chose trajectories with a final apoapsis passage

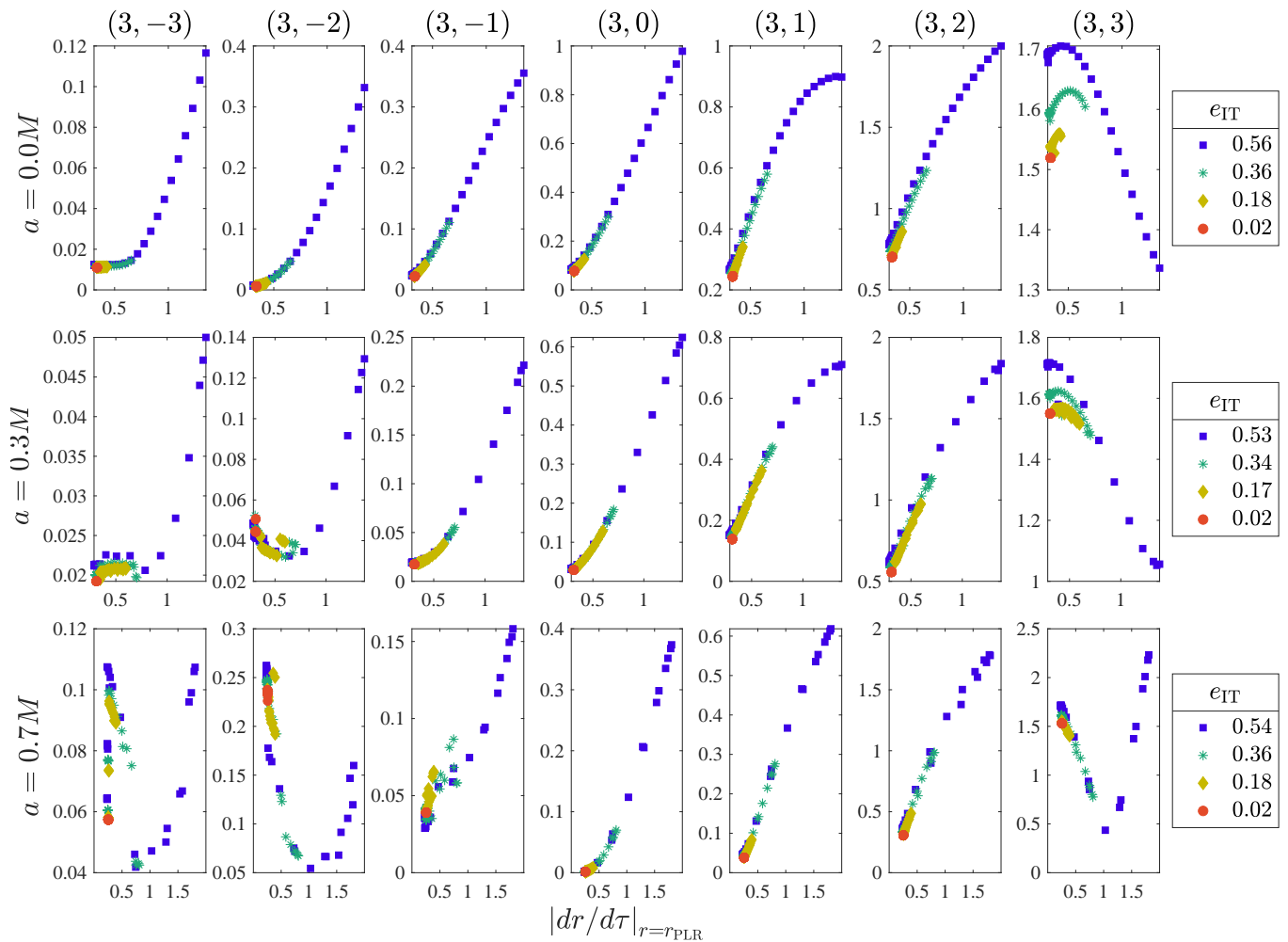


FIG. 10. Mode excitation magnitude \mathcal{A}_{km0} for spheroidal QNMs with $k = 3$, $m \in \{-3, -2, -1, 0, 1, 2, 3\}$, $n = 0$ as a function of radial velocity at the prograde equatorial light ring, $|dr/d\tau|_{r=r_{\text{PLR}}}$. Eccentricities in the strong field vary on the range $e_{\text{IT}} \in [0.01, 0.56]$. Red dots denote the lowest eccentricities, blue squares the highest, and yellow diamonds and green asterisks denote intermediate values. Top panels show results for black hole spin $a = 0$, middle panels $a = 0.3M$, and bottom panels $a = 0.7M$. From left to right, m varies from -3 to 3 . Note that the scale of the vertical axes differs between panels.

at $r \approx 15M$ for ease of comparison between mass ratios.

From this brief study, we can see that mass ratio determines how sensitive the worldlines are to the relativistic anomaly angle: for $\eta = 10^{-3}$, the two behaviors are separated by $\Delta\chi_{r\text{IT}} \approx 23^\circ$; at the more extreme mass ratio, $\Delta\chi_{r\text{IT}} \approx (10^{-8})^\circ$. The different degrees of sensitivity are also apparent by the dephasing in the worldlines: the two trajectories in the bottom panel are so close in $\chi_{r\text{IT}}$ that up until their final orbital cycle, they are indistinguishable at the resolution of this plot; the worldlines in the top panel are out of phase throughout the inspiral. These results, paired with the $\eta = 10^{-4}$ case with $\Delta\chi_{r\text{IT}} \approx (10^{-2})^\circ$ of Sec. IV B 1, indicate that the bifurcation is far more sensitive for EMRI systems than for binaries with more comparable masses.

The quasi-circular motion executed in Fig. 11 (i.e., the

$\Delta t \sim$ several hundred M interval of motion at nearly constant r) is reminiscent of “zoom-whirl” orbit behavior, in which the secondary completes several quasi-circular whirls around the primary during its pericenter passage [192]. As can be seen in Fig. 11, the duration of this whirling increases as the mass ratio approaches the test-mass limit. We can estimate the number of whirls with $N_w = \Delta\phi/2\pi$, where $\Delta\phi$ is the axial angle accumulated during the segment of nearly constant r . For example, for the worldlines with $\eta = 10^{-5}$ in Fig. 11, $N_w = [\phi(t = 1230M) - \phi(t = 790M)]/2\pi$. The $\eta = 10^{-3}$ worldlines shown here have $N_w \approx 1.5$; the $\eta = 10^{-5}$ trajectories have $N_w \approx 6.8$. The more extreme mass-ratio systems exhibit more pronounced zoom-whirl behavior in the strong field than their comparable-mass counterparts. Indeed, the comparable mass systems presented in Ref.

η	a/M	e_{IT}	Bracketing interval $X_{r\text{IT}}^{\text{chif}}$ [deg]
10^{-4}	0	0.27	$353.18 < \chi_{r\text{IT}}^{\text{chif}} < 353.34$
10^{-4}	0	0.46	$355.24 < \chi_{r\text{IT}}^{\text{chif}} < 355.40$
10^{-4}	0	0.67	$356.27 < \chi_{r\text{IT}}^{\text{chif}} < 356.34$
10^{-4}	0.1	0.27	$352.80 < \chi_{r\text{IT}}^{\text{chif}} < 352.96$
10^{-4}	0.1	0.46	$354.98 < \chi_{r\text{IT}}^{\text{chif}} < 355.11$
10^{-4}	0.1	0.67	$356.08 < \chi_{r\text{IT}}^{\text{chif}} < 356.18$
10^{-4}	0.3	0.27	$352.29 < \chi_{r\text{IT}}^{\text{chif}} < 352.48$
10^{-4}	0.3	0.46	$354.72 < \chi_{r\text{IT}}^{\text{chif}} < 354.87$
10^{-4}	0.3	0.67	$355.85 < \chi_{r\text{IT}}^{\text{chif}} < 355.95$
10^{-4}	0.7	0.27	$350.71 < \chi_{r\text{IT}}^{\text{chif}} < 350.93$
10^{-4}	0.7	0.46	$353.81 < \chi_{r\text{IT}}^{\text{chif}} < 353.96$
10^{-4}	0.7	0.67	$355.21 < \chi_{r\text{IT}}^{\text{chif}} < 355.30$
3×10^{-4}	0	0.27	$350.32 < \chi_{r\text{IT}}^{\text{chif}} < 350.59$
3×10^{-4}	0	0.67	$354.80 < \chi_{r\text{IT}}^{\text{chif}} < 355.01$
3×10^{-4}	0.3	0.27	$349.28 < \chi_{r\text{IT}}^{\text{chif}} < 349.55$
3×10^{-4}	0.3	0.67	$354.16 < \chi_{r\text{IT}}^{\text{chif}} < 354.37$
3×10^{-4}	0.7	0.27	$347.06 < \chi_{r\text{IT}}^{\text{chif}} < 347.36$
3×10^{-4}	0.7	0.67	$353.19 < \chi_{r\text{IT}}^{\text{chif}} < 353.40$

TABLE III. Angular intervals $X_{r\text{IT}}^{\text{chif}}$ that bracket the chifurcation for systems with different η, a and e_{IT} .

[141] do not exhibit prolonged quasi-circular kinematics before plunge for any choice of orbital anomaly. The strongly “chifurcating” trajectories are most pronounced in the small mass ratio limit.

We also carried out a brief investigation into the influence of a system’s mass ratio, spin and late-time eccentricity on the chifurcation angle. Although we always find that the chifurcation occurs slightly before periapsis, its precise location can differ between systems with different η, a and e_{IT} . In Table III, we show angular intervals $X_{r\text{IT}}^{\text{chif}}$ that bracket the chifurcation for a variety of systems. For a given η, a and e_{IT} , systems with $\chi_{r\text{IT}}$ at the lower bound of $X_{r\text{IT}}^{\text{chif}}$ execute quasi-circular whirls before plunging, while systems with $\chi_{r\text{IT}}$ at the upper bound of $X_{r\text{IT}}^{\text{chif}}$ move radially outward before plunging. The transition between these two behaviors, the chifurcation, thus occurs at some $\chi_{r\text{IT}} \in X_{r\text{IT}}^{\text{chif}}$. While narrowing the width of each interval $X_{r\text{IT}}^{\text{chif}}$ is possible with repeated calculations, the intervals do not overlap for the cases we wish to compare, so the given resolution of $X_{r\text{IT}}^{\text{chif}}$ is sufficient. The $X_{r\text{IT}}^{\text{chif}}$ intervals in Table III indicate that increasing the spin shifts the chifurcation to smaller $\chi_{r\text{IT}}$, while increasing the eccentricity shifts the chifurcation to larger $\chi_{r\text{IT}}$. Although we only examined two mass ratios, $\eta = 10^{-4}$ and $\eta = 3 \times 10^{-4}$, what we see is that, holding all other parameters constant, making the mass ratio less extreme tends to move the chifurcation to a point earlier than periapsis (i.e., to a somewhat smaller value of $\chi_{r\text{IT}}^{\text{chif}}$).

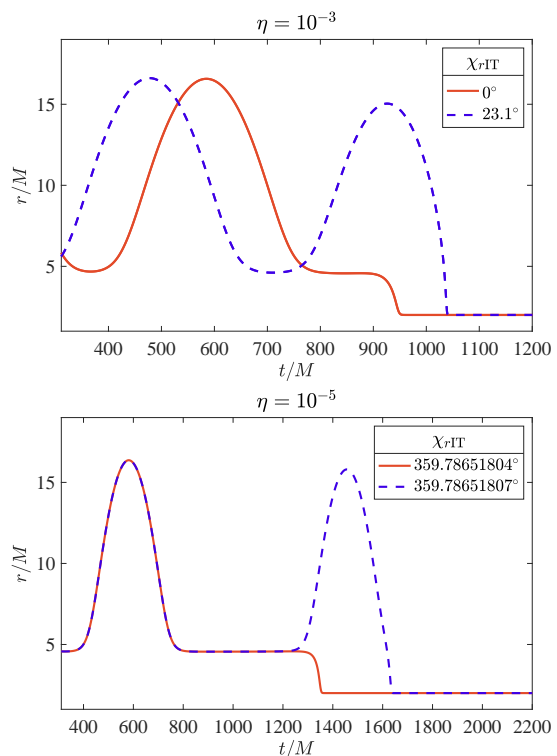


FIG. 11. Worldline sensitivity to the parameter $\chi_{r\text{IT}}$ as a function of mass ratio η . Every worldline corresponds to the inspiral, transition, and plunge of a small body into a Schwarzschild black hole at eccentricity $e_{\text{IT}} = 0.56$. Top panel shows systems with mass ratio $\eta = 10^{-3}$; bottom shows $\eta = 10^{-5}$.

Appendix C: Mode excitation as a function of *ad hoc* model parameter choices

As we stressed in BH25 and recount in Sec. II A, our procedure for generating worldlines relies on two *ad hoc* parameters: a parameter α_{IT} which determines when adiabatic inspiral ends and the transition begins; and a parameter β_{TP} , which sets the end of the transition. See BH25 for the detailed definitions and formulae describing these quantities. In this appendix, we investigate the robustness of our ringdown model against variations in these model parameter choices, focusing on the QNM-dominated regime.

Figure 12 examines how the $k = 2$ QNMs depend on $\alpha_{\text{IT}} \in [0.1, 1.1]$ for a variety of eccentric mergers with $a = 0.7M$ and $\eta = 10^{-4}$. Since the eccentric transition permits two classes of late-time dynamics, we study both scenarios in this figure: systems that complete quasi-circular whirls before the plunge are described by the top panels, and systems that complete a radial cycle before plunging from large radius are in the bottom panels. In both cases, the left five panels show the QNM amplitudes; and the right-most panels show four representative worldlines. While variations in α_{IT} can affect the absolute QNM amplitude, especially in the cases shown in the bot-

tom panels, the relative mode excitation is unchanged: if the $(2, 2)$ mode dominates when $\alpha_{\text{TT}} = 0.1$, it remains the strongest excited mode when $\alpha_{\text{TT}} = 1.1$. Bearing in mind that BH25 recommended holding $0.75 \leq \alpha_{\text{TT}} \leq 1$, we see that the QNM excitations are quite stable against variations in α_{TT} .

Figure 13 examines the $k = 2$ QNM modes as a function of β_{TP} . The left five panels again include the absolute mode amplitudes for $m \in \{-2, \dots, 2\}$, and the right-most panel shows representative worldlines that differ only by β_{TP} . As in Fig. 12, each system has $a = 0.7M$

and $\eta = 10^{-4}$, but now $e_{\text{TT}} \in [0.02, 0.58]$. We see even less variation in the mode amplitudes here than we see when we vary α_{TT} , especially if we focus on the range $0.33 \leq \beta_{\text{TP}} \leq 0.99$ advocated for in BH25. In many cases, the variation cannot be discerned at the resolution of this graphic. We conclude that our ringdown model is also quite stable against changes in β_{TP} .

We do not investigate the dependence of power-law tails on our model parameter choices. Such a study would be computationally expensive. Given the results we find for QNMs, there does not appear to be a significant need for such an investigation.

-
- [1] R. Abbott et al. GWTC-3: Compact Binary Coalescences Observed by LIGO and Virgo during the Second Part of the Third Observing Run. *Physical Review X*, 13(4), December 2023.
 - [2] The LIGO Scientific Collaboration, the Virgo Collaboration, the KAGRA Collaboration, et al. GWTC-4.0: Updating the Gravitational-Wave Transient Catalog with Observations from the First Part of the Fourth LIGO-Virgo-KAGRA Observing Run, 2025.
 - [3] Isobel Romero-Shaw, Paul D. Lasky, and Eric Thrane. Four Eccentric Mergers Increase the Evidence that LIGO-Virgo-KAGRA’s Binary Black Holes Form Dynamically. *The Astrophysical Journal*, 940(2):171, December 2022.
 - [4] Isobel Romero-Shaw, Paul D. Lasky, Eric Thrane, and Juan Calderón Bustillo. GW190521: Orbital Eccentricity and Signatures of Dynamical Formation in a Binary Black Hole Merger Signal. *The Astrophysical Journal Letters*, 903(1):L5, October 2020.
 - [5] Nihar Gupte, Antoni Ramos-Buades, Alessandra Buonanno, Jonathan Gair, M. Coleman Miller, Maximilian Dax, Stephen R. Green, Michael Pürrer, Jonas Wildberger, Jakob Macke, Isobel M. Romero-Shaw, and Bernhard Schölkopf. Evidence for eccentricity in the population of binary black holes observed by LIGO-Virgo-KAGRA, 2024.
 - [6] Hai-Tian Wang, Shao-Peng Tang, Peng-Cheng Li, and Yi-Zhong Fan. Detection of a Higher Harmonic Quasinormal Mode in the Ringdown Signal of GW231123, 2025.
 - [7] A. G. Abac et al. GW241011 and GW241110: Exploring Binary Formation and Fundamental Physics with Asymmetric, High-spin Black Hole Coalescences. *The Astrophysical Journal Letters*, 993(1):L21, October 2025.
 - [8] Pau Amaro-Seoane, Heather Audley, Stanislav Babak, John Baker, Enrico Barausse, Peter Bender, Emanuele Berti, Pierre Binétruy, Michael Born, Daniele Bortoluzzi, Jordan Camp, Chiara Caprini, Vitor Cardoso, Monica Colpi, John Conklin, Neil Cornish, Curt Cutler, Karsten Danzmann, Rita Dolese, Luigi Ferraioli, Valerio Ferroni, Ewan Fitzsimons, Jonathan Gair, Lluís Gesa Bote, Domenico Giardini, Ferran Gibert, Catia Grigiani, Hubert Halloin, Gerhard Heinzl, Thomas Hertog, Martin Hewitson, Kelly Holley-Bockelmann, Daniel Hollington, Mauro Hueller, Henri Inchauspe, Philippe Jetzer, Nikos Karnesis, Christian Killow, Antoine Klein, Bill Klipstein, Natalia Korsakova, Shane L Larson, Jeffrey Livas, Ivan Lloro, Nary Man, Davor Mance, Joseph Martino, Ignacio Mateos, Kirk McKenzie, Sean T McWilliams, Cole Miller, Guido Mueller, Germano Nardini, Gijs Nelemans, Miquel Nofrarias, Antoine Petiteau, Paolo Pivato, Eric Plagnol, Ed Porter, Jens Reiche, David Robertson, Norna Robertson, Elena Rossi, Giuliana Russano, Bernard Schutz, Alberto Sesana, David Shoemaker, Jacob Slutsky, Carlos F. Sopuerta, Tim Sumner, Nicola Tamanini, Ira Thorpe, Michael Troebels, Michele Vallisneri, Alberto Vecchio, Daniele Vetrugno, Stefano Vitale, Marta Volonteri, Gudrun Wanner, Harry Ward, Peter Wass, William Weber, John Ziemer, and Peter Zweifel. Laser Interferometer Space Antenna. *arXiv e-prints*, page arXiv:1702.00786, February 2017.
 - [9] Stanislav Babak, Jonathan Gair, Alberto Sesana, Enrico Barausse, Carlos F. Sopuerta, Christopher P. L. Berry, Emanuele Berti, Pau Amaro-Seoane, Antoine Petiteau, and Antoine Klein. Science with the space-based interferometer LISA. V. Extreme mass-ratio inspirals. *Phys. Rev. D*, 95:103012, May 2017.
 - [10] Monica Colpi et al. LISA Definition Study Report, 2024.
 - [11] Davide Mancieri, Luca Broggi, Morgan Vinciguerra, Alberto Sesana, and Matteo Bonetti. Eccentricity distribution of extreme mass ratio inspirals, 2025.
 - [12] Smadar Naoz, Sanaea C. Rose, Erez Michaely, Denyz Melchior, Enrico Ramirez-Ruiz, Brenna Mockler, and Jeremy D. Schnittman. The Combined Effects of Two-body Relaxation Processes and the Eccentric Kozai-Lidov Mechanism on the Extreme-mass-ratio Inspirals Rate. *The Astrophysical Journal Letters*, 927(1):L18, March 2022.
 - [13] J. Nate Bode and Christopher Wegg. Production of EMRIs in Supermassive Black Hole Binaries, 2013.
 - [14] Elisa Bortolas, Michela Mapelli, and Mario Spera. Supernova kicks and dynamics of compact remnants in the Galactic Centre. *Monthly Notices of the Royal Astronomical Society*, 469(2):1510–1520, April 2017.
 - [15] Elisa Bortolas and Michela Mapelli. Can supernova kicks trigger EMRIs in the galactic centre? *Monthly Notices of the Royal Astronomical Society*, 485(2):2125–2138, February 2019.
 - [16] Davide Mancieri, Luca Broggi, Matteo Bonetti, and Alberto Sesana. Hanging on the cliff: Extreme mass ratio

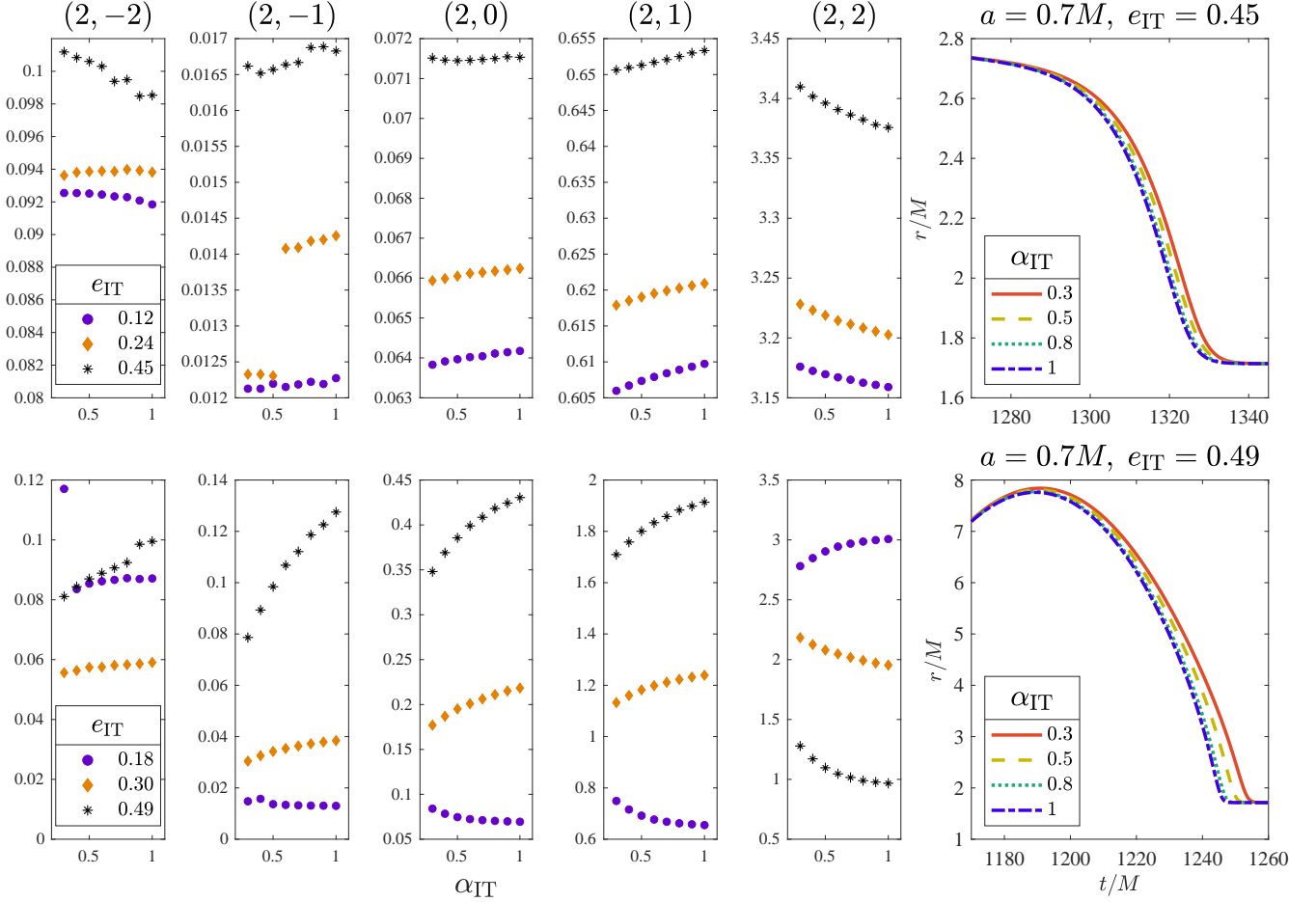


FIG. 12. Mode excitation magnitude \mathcal{A}_{km0} for spheroidal QNMs with $k = 2$, $m \in \{-2, -1, 0, 1, 2\}$, $n = 0$ as a function of α_{IT} . All systems have $a = 0.7M$, $\eta = 10^{-4}$ and $e_{\text{IT}} \in [0.12, 0.49]$. Systems described by the top panels immediately plunge when adiabatic inspiral ends (as depicted by the worldlines in the right-most panel), and systems included in the bottom panels execute one final radial cycle before plunging (as illustrated in the right-most panel).

- inspiral formation with local two-body relaxation and post-newtonian dynamics. *Astronomy & Astrophysics*, 694:A272, February 2025.
- [17] Smadar Naoz and Zoltan Haiman. The Enhanced Population of Extreme Mass-Ratio Inspirals in the LISA Band from Supermassive Black Hole Binaries, 2023.
- [18] Barak Rom, Itai Linial, Karamveer Kaur, and Re'em Sari. Dynamics Around Supermassive Black Holes: Extreme-mass-ratio Inspirals as Gravitational-wave Sources. *The Astrophysical Journal*, 977(1):7, December 2024.
- [19] Michela Mapelli. *Formation Channels of Single and Binary Stellar-Mass Black Holes*, pages 1–65. Springer Singapore, 2021.
- [20] Ilya Mandel and Alison Farmer. Merging stellar-mass binary black holes. *Physics Reports*, 955:1–4, April 2022.
- [21] B. P. Abbott et al. ASTROPHYSICAL IMPLICATIONS OF THE BINARY BLACK HOLE MERGER GW150914. *The Astrophysical Journal Letters*, 818(2):L22, February 2016.
- [22] William J. Smith, Krystal Ruiz-Rocha, Kelly Holley-Bockelmann, Michela Mapelli, and Karan Jani. Probing Binary Black Hole Formation Channels through Cosmic Large-Scale Structure, 2025.
- [23] Houyi Sun, Ya-Ping Li, Zhen Pan, and Huan Yang. Probing Formation Channels of Extreme Mass-Ratio Inspirals, 2025.
- [24] Kyle Kremer. Compact Objects in Globular Clusters, 2025.
- [25] Michael Zevin, Isobel M. Romero-Shaw, Kyle Kremer, Eric Thrane, and Paul D. Lasky. Implications of Eccentric Observations on Binary Black Hole Formation Channels. *The Astrophysical Journal Letters*, 921(2):L43, November 2021.
- [26] Carl L. Rodriguez, Sourav Chatterjee, and Frederic A. Rasio. Binary black hole mergers from globular clusters: Masses, merger rates, and the impact of stellar evolution. *Phys. Rev. D*, 93(8):084029, April 2016.
- [27] Michael Zevin, Johan Samsing, Carl Rodriguez, Carl-Johan Haster, and Enrico Ramirez-Ruiz. Eccentric Black Hole Mergers in Dense Star Clusters: The Role of Binary-Binary Encounters. *The Astrophysical Journal*, 871(1):91, 2019.
- [28] László Gondán and Bence Kocsis. High eccentricities

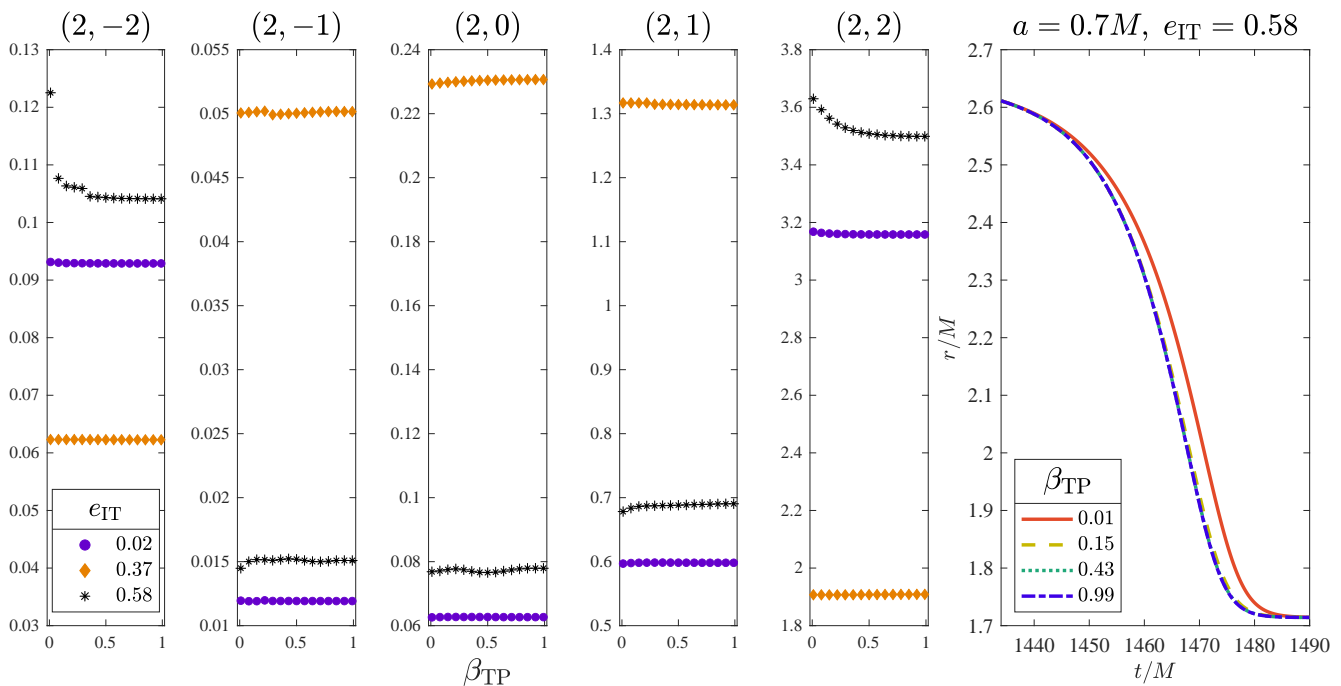


FIG. 13. Mode excitation magnitude \mathcal{A}_{km0} for spheroidal QNMs with $k = 2$, $m \in \{-2, -1, 0, 1, 2\}$, $n = 0$ as a function of β_{TP} . All systems have $a = 0.7M$, $\eta = 10^{-4}$ and $e_{\text{IT}} \in [0.02, 0.58]$. The first five panels show the mode amplitudes, and the right-most panel includes four representative worldlines with different values of β_{TP} .

- and high masses characterize gravitational-wave captures in galactic nuclei as seen by Earth-based detectors. *Monthly Notices of the Royal Astronomical Society*, 506(2):1665–1696, July 2021.
- [29] M. Coleman Miller and Douglas P. Hamilton. Production of intermediate-mass black holes in globular clusters. *Monthly Notices of the Royal Astronomical Society*, 330:232–240, 2001.
- [30] Marco Dall’Amico, Michela Mapelli, Stefano Torniamenti, and Manuel Arca Sedda. Eccentric black hole mergers via three-body interactions in young, globular, and nuclear star clusters. *Astronomy & Astrophysics*, 683:A186, March 2024.
- [31] Kedron Silsbee and Scott Tremaine. Lidov-Kozai Cycles with Gravitational Radiation: Merging Black Holes in Isolated Triple Systems. *The Astrophysical Journal*, 836(1):39, February 2017.
- [32] Manuel Arca Sedda, Gongjie Li, and Bence Kocsis. Order in the chaos: Eccentric black hole binary mergers in triples formed via strong binary-binary scatterings. *Astronomy & Astrophysics*, 650:A189, June 2021.
- [33] Johan Samsing, Morgan MacLeod, and Enrico Ramirez-Ruiz. THE FORMATION OF ECCENTRIC COMPACT BINARY INSPIRALS AND THE ROLE OF GRAVITATIONAL WAVE EMISSION IN BINARY-SINGLE STELLAR ENCOUNTERS. *The Astrophysical Journal*, 784(1):71, March 2014.
- [34] Fabio Antonini, Silvia Toonen, and Adrian S. Hamers. Binary Black Hole Mergers from Field Triples: Properties, Rates, and the Impact of Stellar Evolution. *The Astrophysical Journal*, 841(2):77, May 2017.
- [35] Marta Cocco, Gianluca Grignani, Troels Harmark, Marta Orselli, and Daniele Pica. Strong-gravity precession resonances for binary systems orbiting a Schwarzschild black hole. *Phys. Rev. D*, 112(4):044010, 2025.
- [36] Marta Cocco, Gianluca Grignani, Troels Harmark, Marta Orselli, Davide Panella, and Daniele Pica. Observable signature of magnetic tidal coupling in hierarchical triple systems. October 2025.
- [37] Filippo Camilloni, Troels Harmark, Gianluca Grignani, Marta Orselli, and Daniele Pica. Binary mergers in strong gravity background of Kerr black hole. *Mon. Not. Roy. Astron. Soc.*, 531(1):1884–1904, 2024.
- [38] A. V. Tutukov and L. R. Yungel’Son. Formation of neutron stars in binary systems. *Astronomy Reports*, 37(4):411–431, July 1993.
- [39] Krzysztof Belczynski, Vassiliki Kalogera, and Tomasz Bulik. A Comprehensive Study of Binary Compact Objects as Gravitational Wave Sources: Evolutionary Channels, Rates, and Physical Properties. *Astrophys. J.*, 572(1):407–431, June 2002.
- [40] Krzysztof Belczynski, Daniel E. Holz, Tomasz Bulik, and Richard O’Shaughnessy. The first gravitational-wave source from the isolated evolution of two stars in the 40–100 solar mass range. *Nature*, 534(7608):512–515, June 2016.
- [41] Devin R. Becker and Scott A. Hughes. Transition from adiabatic inspiral to plunge for eccentric binaries. *Phys. Rev. D*, 111:064003, March 2025.
- [42] Amos Ori and Kip S. Thorne. Transition from inspiral to plunge for a compact body in a circular equatorial orbit around a massive, spinning black hole. *Phys. Rev. D*, 62(12):124022, December 2000.

- [43] R. O’Shaughnessy. Transition from inspiral to plunge for eccentric equatorial Kerr orbits. *Physical Review D*, 67(4), February 2003.
- [44] Pranesh A. Sundararajan. Transition from adiabatic inspiral to geodesic plunge for a compact object around a massive Kerr black hole: Generic orbits. *Phys. Rev. D*, 77(12):124050, June 2008.
- [45] Ulrich Sperhake, Emanuele Berti, Vitor Cardoso, José A. González, Bernd Brügmann, and Marcus Ansorg. Eccentric binary black-hole mergers: The transition from inspiral to plunge in general relativity. *Physical Review D*, 78(6), September 2008.
- [46] Simone Albanesi, Sebastiano Bernuzzi, Thibault Damour, Alessandro Nagar, and Andrea Placidi. Faithful effective-one-body waveform of small-mass-ratio coalescing black hole binaries: The eccentric, nonspinning case. *Physical Review D*, 108(8), October 2023.
- [47] Guillaume Lhost and Geoffrey Compère. Approach to the separatrix with eccentric orbits. *SciPost Physics Core*, 8(3), August 2025.
- [48] Loïc Honet, Lorenzo Küchler, Adam Pound, and Geoffrey Compère. Transition-to-plunge self-force waveforms with a spinning primary, 2025.
- [49] Guglielmo Faggioli, Maarten van de Meent, Alessandra Buonanno, and Gaurav Khanna. Characterizing the merger of equatorial-eccentric-geodesic plunges in rotating black holes. *Physical Review D*, 112(8), October 2025.
- [50] Alessandra Buonanno and Thibault Damour. Transition from inspiral to plunge in binary black hole coalescences. *Phys. Rev. D*, 62:064015, Aug 2000.
- [51] Michael Kesden. Transition from adiabatic inspiral to plunge into a spinning black hole. *Physical Review D*, 83(10), May 2011.
- [52] Anuj Apte and Scott A. Hughes. Exciting black hole modes via misaligned coalescences. I. Inspirational, transition, and plunge trajectories using a generalized Ori-Thorne procedure. *Phys. Rev. D*, 100(8):084031, October 2019.
- [53] Ollie Burke, Jonathan Gair, and Joan Simón. Transition from inspiral to plunge: A complete near-extremal trajectory and associated waveform. *Physical Review D*, 101(6), March 2020.
- [54] Geoffrey Compère and Lorenzo Küchler. Self-Consistent Adiabatic Inspirational and Transition Motion. *Phys. Rev. Lett.*, 126(24):241106, June 2021.
- [55] Lorenzo Küchler, Geoffrey Compère, Leanne Durkan, and Adam Pound. Self-force framework for transition-to-plunge waveforms. *arXiv e-prints*, page arXiv:2405.00170, April 2024.
- [56] Lorenzo Küchler, Geoffrey Compère, and Adam Pound. Self-force framework for merger-ringdown waveforms, 2025.
- [57] Adam Pound and Barry Wardell. Black Hole Perturbation Theory and Gravitational Self-Force. In *Handbook of Gravitational Wave Astronomy*, page 38. 2022.
- [58] Saul A. Teukolsky. Perturbations of a Rotating Black Hole. I. Fundamental Equations for Gravitational, Electromagnetic, and Neutrino-Field Perturbations. *Astrophys. J.*, 185:635–648, 1973.
- [59] Pranesh A. Sundararajan, Gaurav Khanna, and Scott A. Hughes. Towards adiabatic waveforms for inspiral into Kerr black holes: A new model of the source for the time domain perturbation equation. *Phys. Rev. D*, 76:104005, Nov 2007.
- [60] Pranesh A. Sundararajan, Gaurav Khanna, Scott A. Hughes, and Steve Drasco. Towards adiabatic waveforms for inspiral into Kerr black holes. II. Dynamical sources and generic orbits. *Phys. Rev. D*, 78:024022, Jul 2008.
- [61] Pranesh A. Sundararajan, Gaurav Khanna, and Scott A. Hughes. Binary black hole merger gravitational waves and recoil in the large mass ratio limit. *Phys. Rev. D*, 81:104009, May 2010.
- [62] Anil Zenginoğlu and Gaurav Khanna. Null Infinity Waveforms from Extreme-Mass-Ratio Inspirals in Kerr Spacetime. *Phys. Rev. X*, 1:021017, December 2011.
- [63] Scott E. Field, Sigal Gottlieb, Zachary J. Grant, Leah F. Isherwood, and Gaurav Khanna. A GPU-Accelerated Mixed-Precision WENO Method for Extremal Black Hole and Gravitational Wave Physics Computations. *Communications on Applied Mathematics and Computation*, 5(1):97–115, May 2021.
- [64] Lior M. Burko and Gaurav Khanna. Gravitational waves from a plunge into a nearly extremal Kerr black hole. *Phys. Rev. D*, 94:084049, October 2016.
- [65] Sarp Akçay, Alexandre Le Tiec, Leor Barack, Norichika Sago, and Niels Warburton. Comparison between self-force and post-Newtonian dynamics: Beyond circular orbits. *Phys. Rev. D*, 91(12):124014, June 2015.
- [66] Barry Wardell, Adam Pound, Niels Warburton, Jeremy Miller, Leanne Durkan, and Alexandre Le Tiec. Gravitational Waveforms for Compact Binaries from Second-Order Self-Force Theory. *Phys. Rev. Lett.*, 130(24):241402, June 2023.
- [67] Alexandre Le Tiec. Perturbative, Post-Newtonian, and General Relativistic Dynamics of Black Hole Binaries, 2011.
- [68] Maarten van de Meent and Harald P. Pfeiffer. Intermediate Mass-Ratio Black Hole Binaries: Applicability of Small Mass-Ratio Perturbation Theory. *Physical Review Letters*, 125(18), October 2020.
- [69] C. V. Vishveshwara. Stability of the Schwarzschild Metric. *Phys. Rev. D*, 1:2870–2879, May 1970.
- [70] William H. Press. Long Wave Trains of Gravitational Waves from a Vibrating Black Hole. *Astrophys. J.*, 170:L105, December 1971.
- [71] S. Chandrasekhar and S. Detweiler. The Quasi-Normal Modes of the Schwarzschild Black Hole. *Proceedings of the Royal Society of London Series A*, 344(1639):441–452, August 1975.
- [72] Edward W. Leaver. Spectral decomposition of the perturbation response of the Schwarzschild geometry. *Phys. Rev. D*, 34:384–408, Jul 1986.
- [73] Hans-Peter Nollert. TOPICAL REVIEW: Quasinormal modes: the characteristic ‘sound’ of black holes and neutron stars. *Classical and Quantum Gravity*, 16(12):R159–R216, December 1999.
- [74] Nils Andersson. Evolving test fields in a black-hole geometry. *Physical Review D*, 55(2):468–479, 1997.
- [75] Tullio Regge and John A. Wheeler. Stability of a Schwarzschild Singularity. *Phys. Rev.*, 108:1063–1069, November 1957.
- [76] Frank J. Zerilli. Effective Potential for Even-Parity Regge-Wheeler Gravitational Perturbation Equations. *Phys. Rev. Lett.*, 24:737–738, March 1970.
- [77] Karl Martel and Eric Poisson. Gravitational perturbations of the Schwarzschild spacetime: A practical co-

- variant and gauge-invariant formalism. *Phys. Rev. D*, 71:104003, May 2005.
- [78] Alessandro Nagar and Luciano Rezzolla. TOPICAL REVIEW: Gauge-invariant non-spherical metric perturbations of Schwarzschild black-hole spacetimes. *Classical and Quantum Gravity*, 22(16):R167–R192, August 2005.
- [79] Marina De Amicis, Enrico Cannizzaro, Gregorio Carullo, and Laura Sberna. Dynamical quasinormal mode excitation, 2025.
- [80] Fernando Echeverria. Gravitational-wave measurements of the mass and angular momentum of a black hole. *Phys. Rev. D*, 40:3194–3203, November 1989.
- [81] Olaf Dreyer, Bernard Kelly, Badri Krishnan, Lee Samuel Finn, David Garrison, and Ramon Lopez-Aleman. Black-hole spectroscopy: testing general relativity through gravitational-wave observations. *Classical and Quantum Gravity*, 21(4):787–803, 2004.
- [82] Emanuele Berti, Vitor Cardoso, and Clifford M. Will. Gravitational-wave spectroscopy of massive black holes with the space interferometer LISA. *Phys. Rev. D*, 73:064030, March 2006.
- [83] Emanuele Berti, Enrico Barausse, Vitor Cardoso, Leonardo Gualtieri, Paolo Pani, Ulrich Sperhake, Leo C Stein, Norbert Wex, Kent Yagi, Tessa Baker, C P Burgess, Flávio S Coelho, Daniela Doneva, Antonio De Felice, Pedro G Ferreira, Paulo C C Freire, James Healy, Carlos Herdeiro, Michael Horbatsch, Burkhard Kleihaus, Antoine Klein, Kostas Kokkotas, Jutta Kunz, Pablo Laguna, Ryan N Lang, Tjonnie G F Li, Tyson Littenberg, Andrew Matas, Saeed Mirshekari, Hirotada Okawa, Eugen Radu, Richard O’Shaughnessy, Bangalore S Sathyaprakash, Chris Van Den Broeck, Hans A Winther, Helvi Witek, Mir Emad Aghili, Justin Alsing, Brett Bolen, Luca Bombelli, Sarah Caudill, Liang Chen, Juan Carlos Degollado, Ryuichi Fujita, Caixia Gao, Davide Gerosa, Saeed Kamali, Hector O Silva, João G Rosa, Laleh Sadeghian, Marco Sampaio, Hajime Sotani, and Miguel Zilhao. Testing general relativity with present and future astrophysical observations. *Classical and Quantum Gravity*, 32(24):243001, December 2015.
- [84] Emanuele Berti, Alberto Sesana, Enrico Barausse, Vitor Cardoso, and Krzysztof Belczynski. Spectroscopy of Kerr Black Holes with Earth- and Space-Based Interferometers. *Phys. Rev. Lett.*, 117:101102, September 2016.
- [85] Eric Thrane, Paul D. Lasky, and Yuri Levin. Challenges for testing the no-hair theorem with current and planned gravitational-wave detectors. *Phys. Rev. D*, 96:102004, November 2017.
- [86] Vishal Baibhav, Emanuele Berti, Vitor Cardoso, and Gaurav Khanna. Black hole spectroscopy: Systematic errors and ringdown energy estimates. *Phys. Rev. D*, 97:044048, February 2018.
- [87] Vishal Baibhav and Emanuele Berti. Multimode black hole spectroscopy. *Phys. Rev. D*, 99:024005, January 2019.
- [88] Maximiliano Isi, Matthew Giesler, Will M. Farr, Mark A. Scheel, and Saul A. Teukolsky. Testing the No-Hair Theorem with GW150914. *Phys. Rev. Lett.*, 123:111102, September 2019.
- [89] Juan Calderón Bustillo, Paul D. Lasky, and Eric Thrane. Black-hole spectroscopy, the no-hair theorem, and GW150914: Kerr versus Occam. *Phys. Rev. D*, 103:024041, January 2021.
- [90] Ioannis Kamaretsos, Mark Hannam, Sascha Husa, and B. S. Sathyaprakash. Black-hole hair loss: Learning about binary progenitors from ringdown signals. *Phys. Rev. D*, 85:024018, January 2012.
- [91] Ioannis Kamaretsos, Mark Hannam, and B. S. Sathyaprakash. Is Black-Hole Ringdown a Memory of Its Progenitor? *Phys. Rev. Lett.*, 109:141102, October 2012.
- [92] Scott A. Hughes and Kristen Menou. Golden Binary Gravitational-Wave Sources: Robust Probes of Strong-Field Gravity. *The Astrophysical Journal*, 623(2):689–699, April 2005.
- [93] Pablo A. Cano, Marina David, and Guido van der Velde. Amplification of new physics in the quasinormal mode spectrum of highly-rotating black holes, 2025.
- [94] Emanuele Berti et al. Black hole spectroscopy: from theory to experiment, 2025.
- [95] Costantino Pacilio, Swetha Bhagwat, Francesco Nobili, and Davide Gerosa. Flexible mapping of ringdown amplitudes for nonprecessing binary black holes. *Phys. Rev. D*, 110:103037, November 2024.
- [96] Halston Lim, Gaurav Khanna, Anuj Apte, and Scott A. Hughes. Exciting black hole modes via misaligned coalescences. II. The mode content of late-time coalescence waveforms. *Phys. Rev. D*, 100(8):084032, 2019.
- [97] Scott A. Hughes, Anuj Apte, Gaurav Khanna, and Halston Lim. Learning about Black Hole Binaries from their Ringdown Spectra. *Phys. Rev. Lett.*, 123(16):161101, 2019.
- [98] Sizheng Ma, Matthew Giesler, Vijay Varma, Mark A. Scheel, and Yanbei Chen. Universal features of gravitational waves emitted by superkick binary black hole systems. *Phys. Rev. D*, 104(8):084003, 2021.
- [99] Hengrui Zhu, Harrison Siegel, Keefe Mitman, Maximiliano Isi, Will M. Farr, Michael Boyle, Nils Deppe, Lawrence E. Kidder, Sizheng Ma, Jordan Moxon, Kyle C. Nelli, Harald P. Pfeiffer, Mark A. Scheel, Saul A. Teukolsky, William Throwe, Vijay Varma, and Nils L. Vu. Black Hole Spectroscopy for Precessing Binary Black Hole Coalescences, 2025.
- [100] Francesco Nobili, Swetha Bhagwat, Costantino Pacilio, and Davide Gerosa. Ringdown mode amplitudes of precessing binary black holes. *Physical Review D*, 112(4), August 2025.
- [101] Luca Nagni, Alessandro Nagar, Rossella Gamba, Simone Albanesi, and Sebastiano Bernuzzi. Binary black hole merger in the extreme mass ratio limit: a multipolar analysis of the inclined orbit case, 2025.
- [102] Thibault Damour and Alessandro Nagar. The Effective One Body description of the Two-Body problem, 2009.
- [103] Gregorio Carullo. Ringdown amplitudes of nonspinning eccentric binaries. *Journal of Cosmology and Astroparticle Physics*, 2024(10):061, 2024.
- [104] Giuseppe Ficarra and Carlos O. Lousto. Eccentric binary black hole simulations with numerical relativity. *Phys. Rev. D*, 111:044015, February 2025.
- [105] Richard H. Price. Nonspherical Perturbations of Relativistic Gravitational Collapse. I. Scalar and Gravitational Perturbations. *Phys. Rev. D*, 5:2419–2438, May 1972.
- [106] Richard H. Price. Nonspherical Perturbations of Relativistic Gravitational Collapse. II. Integer-Spin, Zero-

- Rest-Mass Fields. *Phys. Rev. D*, 5:2439–2454, May 1972.
- [107] Bryce S. DeWitt and Robert W. Brehme. Radiation damping in a gravitational field. *Annals Phys.*, 9:220–259, 1960.
- [108] E. S. C. Ching, P. T. Leung, W. M. Suen, and K. Young. Wave propagation in gravitational systems: Late time behavior. *Phys. Rev. D*, 52:2118–2132, August 1995.
- [109] Marc Casals and Adrian Ottewill. Spectroscopy of the Schwarzschild Black Hole at Arbitrary Frequencies. *Phys. Rev. Lett.*, 109:111101, September 2012.
- [110] Marina De Amicis, Simone Albanesi, and Gregorio Carullo. Inspiral-inherited ringdown tails. *Phys. Rev. D*, 110:104005, November 2024.
- [111] C. T. Cunningham, R. H. Price, and V. Moncrief. Radiation from collapsing relativistic stars. I. Linearized odd-parity radiation. *Astrophys. J.*, 224:643–667, September 1978.
- [112] Carsten Gundlach, Richard H. Price, and Jorge Pullin. Late-time behavior of stellar collapse and explosions. I. Linearized perturbations. *Phys. Rev. D*, 49:883–889, January 1994.
- [113] Carsten Gundlach, Richard H. Price, and Jorge Pullin. Late-time behavior of stellar collapse and explosions. II. Nonlinear evolution. *Phys. Rev. D*, 49:890–899, January 1994.
- [114] Satoshi Okuzumi, Kunihito Ioka, and Masa-aki Sakagami. Possible discovery of a nonlinear tail and second-order quasinormal modes in black hole ringdown. *Phys. Rev. D*, 77:124018, June 2008.
- [115] Lior M. Burko and Amos Ori. Late-time evolution of nonlinear gravitational collapse. *Phys. Rev. D*, 56:7820–7832, December 1997.
- [116] Leor Barack. Late time decay of scalar, electromagnetic, and gravitational perturbations outside rotating black holes. *Phys. Rev. D*, 61:024026, December 1999.
- [117] Sebastiano Bernuzzi, Alessandro Nagar, and Roberto De Pietri. Dynamical excitation of space-time modes of compact objects. *Physical Review D*, 77(4), February 2008.
- [118] Lior M. Burko and Gaurav Khanna. Mode coupling mechanism for late-time Kerr tails. *Phys. Rev. D*, 89:044037, Feb 2014.
- [119] Anil Zenginoglu, Gaurav Khanna, and Lior M. Burko. Intermediate behavior of Kerr tails. *General Relativity and Gravitation*, 46(3), February 2014.
- [120] Vitor Cardoso, Gregorio Carullo, Marina De Amicis, Francisco Duque, Takuya Katagiri, David Pereñiguez, Jaime Redondo-Yuste, Thomas F. M. Spieksma, and Zhen Zhong. Hushing black holes: Tails in dynamical spacetimes. *Phys. Rev. D*, 109:L121502, Jun 2024.
- [121] Lior M. Burko and Gaurav Khanna. Late-time Kerr tails: generic and non-generic initial data sets, ‘up’ modes, and superposition. *Classical and Quantum Gravity*, 28(2):025012, 2011.
- [122] Lior M. Burko and Gaurav Khanna. Universality of massive scalar field late-time tails in black-hole spacetimes. *Phys. Rev. D*, 70:044018, August 2004.
- [123] Lior M. Burko and Gaurav Khanna. Late-time Kerr tails revisited. *Classical and Quantum Gravity*, 26(1):015014, December 2008.
- [124] William Krivan. Late-time dynamics of scalar fields on rotating black hole backgrounds. *Phys. Rev. D*, 60:101501, October 1999.
- [125] Eric Poisson. Radiative falloff of a scalar field in a weakly curved spacetime without symmetries. *Phys. Rev. D*, 66:044008, August 2002.
- [126] Lior M. Burko and Gaurav Khanna. Radiative falloff in the background of rotating black holes. *Phys. Rev. D*, 67:081502, April 2003.
- [127] Leor Barack and Amos Ori. Late-Time Decay of Scalar Perturbations Outside Rotating Black Holes. *Phys. Rev. Lett.*, 82:4388–4391, May 1999.
- [128] István Rácz and Gábor Zs Tóth. Numerical investigation of the late-time Kerr tails. *Classical and Quantum Gravity*, 28(19):195003, September 2011.
- [129] Enno Harms, Sebastiano Bernuzzi, and Bernd Brügmann. Numerical solution of the $2 + 1$ Teukolsky equation on a hyperboloidal and horizon penetrating foliation of Kerr and application to late-time decays. *Classical and Quantum Gravity*, 30(11):115013, May 2013.
- [130] Anil Zenginoglu. Asymptotics of Schwarzschild black hole perturbations. *Classical and Quantum Gravity*, 27(4):045015, January 2010.
- [131] Shahar Hod. Radiative Tail of Realistic Rotating Gravitational Collapse. *Phys. Rev. Lett.*, 84:10–13, January 2000.
- [132] Tousif Islam, Guglielmo Faggioli, Gaurav Khanna, Scott Field, Maarten van de Meent, and Alessandra Buonanno. Phenomenology and origin of late-time tails in eccentric binary black hole mergers. July 2024.
- [133] Tousif Islam, Guglielmo Faggioli, and Gaurav Khanna. Bayesian analysis of late-time tails in eccentric spinning binary black hole mergers. December 2025.
- [134] Marina De Amicis, Hannes Rüter, Gregorio Carullo, Simone Albanesi, C. Melize Ferrus, Keefe Mitman, Leo C. Stein, Vitor Cardoso, Sebastiano Bernuzzi, Michael Boyle, Nils Deppe, Lawrence E. Kidder, Jordan Moxon, Alessandro Nagar, Kyle C. Nelli, Harald P. Pfeiffer, Mark A. Scheel, William Throwe, Nils L. Vu, and Anil Zenginoglu. Late-time tails in nonlinear evolutions of merging black holes, 2024.
- [135] Sizheng Ma, Mark A. Scheel, Jordan Moxon, Kyle C. Nelli, Nils Deppe, Lawrence E. Kidder, William Throwe, and Nils L. Vu. Merging black holes with Cauchy-characteristic matching: Computation of late-time tails. *Physical Review D*, 112(2), July 2025.
- [136] James Healy and Carlos O. Lousto. Fourth RIT binary black hole simulations catalog: Extension to eccentric orbits. *Phys. Rev. D*, 105:124010, June 2022.
- [137] Michael Boyle, Daniel Hemberger, Dante A B Iozzo, Geoffrey Lovelace, Serguei Ossokine, Harald P Pfeiffer, Mark A Scheel, Leo C Stein, Charles J Woodford, Aaron B Zimmerman, Nousha Afshari, Kevin Barkett, Jonathan Blackman, Katerina Chatziioannou, Tony Chu, Nicholas Demos, Nils Deppe, Scott E Field, Nils L Fischer, Evan Foley, Heather Fong, Alyssa Garcia, Matthew Giesler, François Hébert, Ian Hinder, Reza Katebi, Haroon Khan, Lawrence E Kidder, Prayush Kumar, Kevin Kuper, Halston Lim, Maria Okounkova, Teresita Ramirez, Samuel Rodriguez, Hannes R Rüter, Patricia Schmidt, Bela Szilagyi, Saul A Teukolsky, Vijay Varma, and Marissa Walker. The SXS collaboration catalog of binary black hole simulations. *Classical and Quantum Gravity*, 36(19):195006, September 2019.
- [138] Mark A. Scheel, Michael Boyle, Keefe Mitman, Nils Deppe, Leo C. Stein, Cristóbal Armaza, Marce-

- line S. Bonilla, Luisa T. Buchman, Andrea Ceja, Himanshu Chaudhary, Yitian Chen, Maxence Corman, Károly Zoltán Csukás, C. Melize Ferrus, Scott E. Field, Matthew Giesler, Sarah Habib, François Hébert, Daniel A. Hemberger, Dante A. B. Iozzo, Tousif Islam, Ken Z. Jones, Aniket Khairnar, Lawrence E. Kidder, Taylor Knapp, Prayush Kumar, Guillermo Lara, Oliver Long, Geoffrey Lovelace, Sizheng Ma, Denyz Melchor, Marlo Morales, Jordan Moxon, Peter James Nee, Kyle C. Nelli, Eamonn O'Shea, Serguei Ossokine, Robert Owen, Harald P. Pfeiffer, Isabella G. Pretto, Teresita Ramirez-Aguilar, Antoni Ramos-Buades, Adhrit Ravichandran, Abhishek Ravishankar, Samuel Rodriguez, Hannes R. Rüter, Jennifer Sanchez, Md Arif Shaikh, Dongze Sun, Béla Szilágyi, Daniel Tellez, Saul A. Teukolsky, Sierra Thomas, William Throwe, Vijay Varma, Nils L. Vu, Marissa Walker, Nikolas A. Wittek, and Jooheon Yoo. The SXS Collaboration's third catalog of binary black hole simulations, 2025.
- [139] Sarah Habib, Mark Scheel, and Saul Teukolsky. Eccentricity Reduction for Quasicircular Binary Evolutions, 2024.
- [140] Taylor Knapp, Katerina Chatziioannou, Harald Pfeiffer, Mark A. Scheel, and Lawrence E. Kidder. Parameter control for eccentric, precessing binary black hole simulations with SpEC. *Physical Review D*, 111(2), 2025.
- [141] Peter James Nee, Aldo Gamboa, Harald P Pfeiffer, Lorenzo Pompili, Antoni Ramos-Buades, Vijay Varma, Michael Boyle, Alessandra Buonanno, Raffi Enficiaud, Lawrence E Kidder, and Mark A Scheel. Impact of eccentricity and mean anomaly in numerical relativity mergers. *Classical and Quantum Gravity*, 42(13):135011, July 2025.
- [142] Gaurav Khanna and Richard H. Price. Black hole ringing, quasinormal modes, and light rings. *Phys. Rev. D*, 95:081501, April 2017.
- [143] Richard H. Price, Sourabh Nampalliwar, and Gaurav Khanna. Black hole binary inspiral: Analysis of the plunge. *Phys. Rev. D*, 93:044060, February 2016.
- [144] Roy P. Kerr. Gravitational Field of a Spinning Mass as an Example of Algebraically Special Metrics. *Phys. Rev. Lett.*, 11(5):237–238, September 1963.
- [145] Robert H. Boyer and Richard W. Lindquist. Maximal analytic extension of the Kerr metric. *J. Math. Phys.*, 8:265, 1967.
- [146] Alvin J. K. Chua, Michael L. Katz, Niels Warburton, and Scott A. Hughes. Rapid Generation of Fully Relativistic Extreme-Mass-Ratio-Inspiral Waveform Templates for LISA Data Analysis. *Phys. Rev. Lett.*, 126(5):051102, February 2021.
- [147] Michael L. Katz, Alvin J. K. Chua, Lorenzo Speri, Niels Warburton, and Scott A. Hughes. Fast extreme-mass-ratio-inspiral waveforms: New tools for millihertz gravitational-wave data analysis. *Phys. Rev. D*, 104(6):064047, September 2021.
- [148] Lorenzo Speri, Michael L. Katz, Alvin J. K. Chua, Scott A. Hughes, Niels Warburton, Jonathan E. Thompson, Christian E. A. Chapman-Bird, and Jonathan R. Gair. Fast and Fourier: Extreme Mass Ratio Inspiral Waveforms in the Frequency Domain. *arXiv e-prints*, page arXiv:2307.12585, July 2023.
- [149] Scott A. Hughes, Niels Warburton, Gaurav Khanna, Alvin J. K. Chua, and Michael L. Katz. Adiabatic waveforms for extreme mass-ratio inspirals via multi-voice decomposition in time and frequency. *Phys. Rev. D*, 103(10):104014, May 2021.
- [150] Christian E. A. Chapman-Bird, Lorenzo Speri, Zachary Nasipak, Ollie Burke, Michael L. Katz, Alessandro Santini, Shubham Kejriwal, Philip Lynch, Josh Mathews, Hassan Khalvati, Jonathan E. Thompson, Soichiro Isoyama, Scott A. Hughes, Niels Warburton, Alvin J. K. Chua, and Maxime Pigou. The Fast and the Frame-Dragging: Efficient waveforms for asymmetric-mass eccentric equatorial inspirals into rapidly-spinning black holes, 2025.
- [151] Charles W. Misner, Kip S. Thorne, and John A. Wheeler. *Gravitation*. W. H. Freeman, San Francisco, 1973.
- [152] Curt Cutler, Daniel Kennefick, and Eric Poisson. Gravitational radiation reaction for bound motion around a Schwarzschild black hole. *Phys. Rev. D*, 50(6):3816–3835, September 1994.
- [153] Ezra Newman and Roger Penrose. An Approach to gravitational radiation by a method of spin coefficients. *J. Math. Phys.*, 3:566–578, 1962.
- [154] J. N. Goldberg, A. J. Macfarlane, E. T. Newman, F. Rohrlich, and E. C. G. Sudarshan. Spin-s Spherical Harmonics and $\bar{\delta}$. *Journal of Mathematical Physics*, 8(11):2155–2161, November 1967.
- [155] Emanuele Berti, Vitor Cardoso, and Andrei O Starinets. Quasinormal modes of black holes and black branes. *Classical and Quantum Gravity*, 26(16):163001, July 2009.
- [156] William H. Press and Saul A. Teukolsky. Perturbations of a Rotating Black Hole. II. Dynamical Stability of the Kerr Metric. *Astrophys. J.*, 185:649–674, 1973.
- [157] Leo C. Stein. qnm: A Python package for calculating Kerr quasinormal modes, separation constants, and spherical-spheroidal mixing coefficients. *J. Open Source Softw.*, 4(42):1683, 2019.
- [158] Arnab Dhani. Importance of mirror modes in binary black hole ringdown waveform. *Phys. Rev. D*, 103:104048, May 2021.
- [159] Ernst Nils Dorband, Emanuele Berti, Peter Diener, Erik Schnetter, and Manuel Tiglio. Numerical study of the quasinormal mode excitation of Kerr black holes. *Phys. Rev. D*, 74:084028, October 2006.
- [160] Emanuele Berti and Vitor Cardoso. Quasinormal ringing of Kerr black holes: The excitation factors. *Phys. Rev. D*, 74:104020, November 2006.
- [161] Alessandra Buonanno, Gregory B. Cook, and Frans Pretorius. Inspiral, merger, and ring-down of equal-mass black-hole binaries. *Phys. Rev. D*, 75:124018, June 2007.
- [162] Lionel London, Deirdre Shoemaker, and James Healy. Modeling ringdown: Beyond the fundamental quasinormal modes. *Phys. Rev. D*, 90:124032, December 2014.
- [163] L. T. London, James Healy, and Deirdre Shoemaker. Erratum: Modeling ringdown: Beyond the fundamental quasinormal modes [Phys. Rev. D 90, 124032 (2014)]. *Phys. Rev. D*, 94:069902, September 2016.
- [164] L. London. Modeling ringdown. II. Aligned-spin binary black holes, implications for data analysis and fundamental theory. *Phys. Rev. D*, 102:084052, October 2020.
- [165] Keefe Mitman, Isabella Pretto, Harrison Siegel, Mark A. Scheel, Saul A. Teukolsky, Michael Boyle, Nils Deppe, Lawrence E. Kidder, Jordan Moxon, Kyle C. Nelli, William Throwe, and Nils L. Vu. Probing the ring-

- down perturbation in binary black hole coalescences with an improved quasi-normal mode extraction algorithm, 2025.
- [166] Mark Ho-Yeuk Cheung, Emanuele Berti, Vishal Baibhav, and Roberto Cotesta. Extracting linear and nonlinear quasinormal modes from black hole merger simulations. *Physical Review D*, 109(4), February 2024.
- [167] Hengrui Zhu, Justin L. Ripley, Alejandro Cárdenas-Avendaño, and Frans Pretorius. Challenges in quasinormal mode extraction: Perspectives from numerical solutions to the Teukolsky equation. *Physical Review D*, 109(4), February 2024.
- [168] Vishal Baibhav, Mark Ho-Yeuk Cheung, Emanuele Berti, Vitor Cardoso, Gregorio Carullo, Roberto Cotesta, Walter Del Pozzo, and Francisco Duque. Agnostic black hole spectroscopy: Quasinormal mode content of numerical relativity waveforms and limits of validity of linear perturbation theory. *Physical Review D*, 108(10), November 2023.
- [169] Keefe Mitman, Macarena Lagos, Leo C. Stein, Sizheng Ma, Lam Hui, Yanbei Chen, Nils Deppe, François Hébert, Lawrence E. Kidder, Jordan Moxon, Mark A. Scheel, Saul A. Teukolsky, William Throwe, and Nils L. Vu. Nonlinearities in Black Hole Ringdowns. *Phys. Rev. Lett.*, 130:081402, February 2023.
- [170] Mark Ho-Yeuk Cheung, Vishal Baibhav, Emanuele Berti, Vitor Cardoso, Gregorio Carullo, Roberto Cotesta, Walter Del Pozzo, Francisco Duque, Thomas Helfer, Estuti Shukla, and Kaze W.K. Wong. Nonlinear Effects in Black Hole Ringdown. *Physical Review Letters*, 130(8), February 2023.
- [171] Peter James Nee, Sebastian H. Völkel, and Harald P. Pfeiffer. Role of black hole quasinormal mode overtones for ringdown analysis. *Phys. Rev. D*, 108:044032, August 2023.
- [172] Swetha Bhagwat, Xisco Jiménez Forteza, Paolo Pani, and Valeria Ferrari. Ringdown overtones, black hole spectroscopy, and no-hair theorem tests. *Phys. Rev. D*, 101:044033, February 2020.
- [173] Bernard J. Kelly and John G. Baker. Decoding mode mixing in black-hole merger ringdown. *Phys. Rev. D*, 87:084004, April 2013.
- [174] Emanuele Berti and Antoine Klein. Mixing of spherical and spheroidal modes in perturbed Kerr black holes. *Phys. Rev. D*, 90:064012, September 2014.
- [175] Gregory B. Cook and Maxim Zaltowski. Gravitational perturbations of the Kerr geometry: High-accuracy study. *Physical Review D*, 90(12), December 2014.
- [176] Andrea Taracchini, Alessandra Buonanno, Gaurav Khanna, and Scott A. Hughes. Small mass plunging into a Kerr black hole: Anatomy of the inspiral-merger-ringdown waveforms. *Physical Review D*, 90(8), October 2014.
- [177] L London and E Fauchon-Jones. On modeling for Kerr black holes: basis learning, QNM frequencies, and spherical-spheroidal mixing coefficients. *Classical and Quantum Gravity*, 36(23):235015, November 2019.
- [178] Scott A. Hughes. The evolution of circular, non-equatorial orbits of Kerr black holes due to gravitational-wave emission, 2000.
- [179] Scott A. Hughes. Erratum: Evolution of circular, nonequatorial orbits of Kerr black holes due to gravitational-wave emission [Phys. Rev. D 61, 084004 (2000)]. *Phys. Rev. D*, 67:089901, April 2003.
- [180] Shahar Hod. Mode coupling in rotating gravitational collapse: Gravitational and electromagnetic perturbations. *Physical Review D*, 61(6), February 2000.
- [181] Carsten Gundlach, Sarp Akcay, Leor Barack, and Alessandro Nagar. Critical phenomena at the threshold of immediate merger in binary black hole systems: The extreme mass ratio case. *Physical Review D*, 86(8), 2012.
- [182] Janna Levin, Rachel O'Reilly, and E. J. Copeland. Gravity waves from homoclinic orbits of compact binaries. *Phys. Rev. D*, 62:024023, June 2000.
- [183] Janna Levin and Gabe Perez-Giz. Homoclinic orbits around spinning black holes. I. Exact solution for the Kerr separatrix. *Phys. Rev. D*, 79:124013, June 2009.
- [184] Lisa V. Drummond, Philip Lynch, Alexandra G. Hanselman, Devin R. Becker, and Scott A. Hughes. Extreme mass-ratio inspiral and waveforms for a spinning body into a Kerr black hole via osculating geodesics and near-identity transformations. *Physical Review D*, 109(6), March 2024.
- [185] Gabriel Andres Piovano, Christiana Pantelidou, Jake Mac Uilliam, and Vojtěch Witzany. Spinning particles near Kerr black holes: Orbits and gravitational-wave fluxes through the Hamilton-Jacobi formalism, 2024.
- [186] Josh Mathews and Adam Pound. Post-adiabatic waveform-generation framework for asymmetric precessing binaries, 2025.
- [187] Viktor Skoupý, Gabriel Andres Piovano, and Vojtěch Witzany. Spherical inspirals of spinning bodies into Kerr black holes, 2025.
- [188] R. O'Shaughnessy, L. London, J. Healy, and D. Shoemaker. Precession during merger: Strong polarization changes are observationally accessible features of strong-field gravity during binary black hole merger. *Phys. Rev. D*, 87:044038, February 2013.
- [189] R. Abbott et al. GW190521: A Binary Black Hole Merger with a Total Mass of $150 M_{\odot}$. *Physical Review Letters*, 125(10), September 2020.
- [190] The LIGO Scientific Collaboration, the Virgo Collaboration, the KAGRA Collaboration, et al. GW231123: a Binary Black Hole Merger with Total Mass $190\text{-}265 M_{\odot}$, 2025.
- [191] Ole Tange. GNU Parallel - The Command-Line Power Tool. *login: The USENIX Magazine*, 36(1):42-47, February 2011.
- [192] Kostas Glampedakis and Daniel Kennefick. Zoom and whirl: Eccentric equatorial orbits around spinning black holes and their evolution under gravitational radiation reaction. *Physical Review D*, 66(4), August 2002.